

Algorithm Theoretical Basis Document for Derived Products Land Surface Temperature (DLST)

PRODUCTS: LSA-003

The EUMETSAT
Network of
Satellite Application
Facilities



Reference Number:
Issue/Revision Index:
Last Change:

SAF/LAND/IM/ATBD_DLST/1.1
Issue 3
02/06/2017

DOCUMENT SIGNATURE TABLE

	Name	Date	Signature
Prepared by :	F. Götttsche		
Approved by :	LSA SAF Project Manager (IPMA)		

DOCUMENTATION CHANGE RECORD

Issue / Revision	Date	Description:
Version 1.0	06/06/2014	Version submitted to EUM Secretariat for verification
Version 1.1	06/11/2015	Version revised considering EUM Secretariat suggestions. Submitted to PCR
Issue 2	01/04/2016	Version updated following the PCR evaluation board recommendations: document structure revised following standards for ATBD; added Figure 1 (processing chains); Tables 1 and 2 updated; removed equation 8; reorganised mathematical description of the algorithm; section on error budget estimation now added; adjusted displayed range in figure 15; added section on assumptions and limitations; changed text to clarify points raised by reviewers; references updated; typos corrected.
Issue 3	02/06/2017	Added annex with description of Processing Scheme (removed from product PUM).

DISTRIBUTION LIST

Internal Consortium Distribution		
Organisation	Name	No. Copies
IPMA	Isabel Trigo	
IPMA	Luís Pessanha	
IPMA	Sandra Coelho Freitas	
IPMA	Isabel Monteiro	
IPMA	Carla Barroso	
IPMA	João Paulo Martins	
IPMA	Pedro Diegues	
IPMA	Benvinda Barbosa	
IPMA	Ana Veloso	
IDL	Carlos da Camara	
IDL	Teresa Calado	
IDL	Sofia Ermida	
KIT	Folke-S. Olesen	
KIT	Frank Goettsche	
MF	Jean-Louis Roujean	
MF	Xavier Ceamanos	
MF	Dominique Carrer	
MF	Gregoire Jacob	
RMI	Françoise Meulenberghs	
RMI	Arboleda Alirio	
RMI	Nicolas Ghilain	
UV	Joaquin Melia	
UV	F. Javier García Haro	
UV/EOLAB	Fernando Camacho	
UV	Aleixander Verger	

External Distribution		
Organisation	Name	No. Copies
EUMETSAT	Frédéric Gasiglia	
EUMETSAT	Dominique Faucher	
EUMETSAT	Lorenzo Sarlo	
EUMETSAT	Lothar Schueller	
EDISOFT	Teresa Cardoso	
EDISOFT	Carlos Vicente	
EDISOFT	Joaquim Araújo	
GMV	Mauro Lima	

Steering Group Distribution		
Nominated by:	Name	No. Copies
IPMA	Pedro Viterbo	
EUMETSAT	Lorenzo Sarlo	
EUMETSAT	Lothar Schueller	
EUMETSAT	Christopher Hanson	
EUMETSAT	Harald Rothfuss	
STG/AFG (USAM)	Francesco Zauli	
MF	Jean-François Mahfouf	
RMI	Rafiq Hamdi	
KIT	Johannes Orphal	
VITO	Bart Deronde	

Table of Contents

DOCUMENT SIGNATURE TABLE	2
DOCUMENTATION CHANGE RECORD	2
1. Introduction	8
2. Algorithm Overview	11
2.1. LST Composites as Input to LSA-003B Algorithm	12
3. Algorithm Description	16
3.1. Theoretical Description	16
3.1.1. Physics of the Problem	16
3.1.2. Mathematical Description of the Algorithm	18
3.1.3. Error Budget Estimates	23
3.2. Practical Considerations	23
3.2.1. Validation and Algorithm Performance	24
3.2.2. Quality Control & Diagnostics	35
3.2.3. Exception Handling	35
3.2.4. Outputs	35
4. Assumptions and Limitations	36
4.1. Assumptions	36
4.2. Constraints and Limitations	36
5. References	38
Annex - Derived LST Composite Products: LSA-003 (DLST) Processing Scheme	

List of Tables

Table 1 Required inputs and purpose of DLST sub-products LSA-003A and LSA-003B.	12
Table 2 Meaning of the model parameters in the Goe2001 and Goe2009 models.	17

List of Figures

Figure 1 Processing chains of the decadal LST (DLST) algorithms (LSA-003). Left: Temporal LST composites (LSA-003A). Right: Thermal Surface Parameters (TSP) algorithm (LSA-003B). The TSP algorithm fits a model of the diurnal temperature cycle (DTC) to DLST composites. The DTC model and the TSP are explained in Figure 6 and Table 2.	12
Figure 2 Maximum LST for 13:00h UTC derived from the first 10 days of August 2010.	13
Figure 3 Median LST for 13:00h UTC derived from the first 10 days of August 2010.	14
Figure 4 Number of valid LST found at 13:00h UTC during the first 10 days of August 2010.	15
Figure 5 Errors associated with maximum LST at 13:00h UTC for the first 10 days of August 2010.	15
Figure 6 Model parameters (Table 2) and fits of the DTC model “Goe2009” (solid line, eq. (16)) and of the Göttsche and Olesen (2001) model “Goe2001” (broken line) to sample LST (data omitted for clarity). The “daytime” part T_1 (sunrise to start of attenuation function at t_s) and the “night-time” part T_2 (t_s to end, here 03:00h) of the models are indicated by broken vertical lines.	17
Figure 7 Mean error at 15min interval over 54 days between LST derived from KT-15 East and fitted LST for Goe2001 (triangles) and Goe2009 with Vollmer airmass definition (crosses) at Gobabeb (05.12.2007 to 28.01.2008).	24
Figure 8 Mean error at 15min interval over 54 days between LST derived from KT-15 East and fitted LST for Goe2009 with airmass definitions according to Vollmer (crosses), simple (diamonds), and Kasten1989 (triangles) at Gobabeb, Namibia (05.12.2007 to 28.01.2008).	25
Figure 9 Histogram of mean absolute deviation per day for Goe2009 with Vollmer airmass definition fitted to 54 diurnal temperature cycles measured at Gobabeb, Namibia.	26
Figure 10 Mean error at 15min interval over 100 days between KT-15 LST and fitted LST for Goe2001 (triangles) and Goe2009 with Vollmer airmass definition (crosses) at Evora, Portugal (11.06.2008 to 08.11.2008).	27
Figure 11 Histogram of mean absolute deviation per day for Goe2009 with Vollmer airmass definition fitted to 100 diurnal temperature cycles measured at Evora, Portugal.	28
Figure 12 Modelled maximum LST for median DTC of the last 10 days in June 2009.	29
Figure 13 Modelled minimum LST for median DTC of the last 10 days in June 2009.	29
Figure 14 Modelled LST amplitude for median DTC of the last 10 days in June 2009.	30
Figure 15 Modelled time of LST maximum for median DTC of the last 10 days in June 2009.	31

Figure 16 Median LST composite at 10:15 UTC obtained for 1-10 October 2009.	32
Figure 17 Maximum temperatures Tmax obtained from median DTC for 1-10 October 2009.	32
Figure 18 Minimum temperatures T0 obtained from median DTC for 1-10 October 2009.	33
Figure 19 Temperature amplitudes ($T_{max} - T_0$) obtained from median DTC for 1-10 October 2009.	34
Figure 20 Subset of Figure 19 showing parts South Africa & Namibia (left) and corresponding Landsat 'true colour image' (right).	34

1. Introduction

The EUMETSAT Satellite Application Facility on Land Surface Analysis (LSA SAF) generates, on an operational basis, Land Surface Temperature (LST) from the Spinning Enhanced Visible and Infrared Imager (SEVIRI) onboard Meteosat Second Generation (MSG) satellites (Schmetz et al., 2002). LST is an important parameter for the monitoring of surface energy budget, since it is the primary variable determining the upward thermal radiation and one of the main controllers of sensible and latent heat fluxes between the surface and the atmosphere. Thus, the reliable and long-term estimation of LST is extremely important for a wide number of applications, including: (i) model validation (Trigo and Viterbo, 2003; Mitchell et al. 2004), (ii) data assimilation (Caparrini et al., 2004; Qin et al, 2007; Bosilovich et al., 2007); (iii) hydrological applications (Kustas et al., 1996; Wan et al., 2004); and (iv) climate monitoring (Jin, 2004; Jin et al., 2005, Yu et al, 2008). LSA SAF MLST (LSA-001) is processed at the full SEVIRI temporal and spatial resolution allowing the capture of the full diurnal cycle over clear sky regions. The LSA-003 product ‘Derived Products Land Surface Temperature (DLST)’ presented here is entirely derived from LSA SAF’s MLST product (LSA-001). Details on the MLST product and its performance are given in the ‘Algorithm Theoretical Basis Document (ATBD) for LST’ (Trigo et al., 2009), the ‘Product User Manual (PUM) Land Surface Temperature’ (Land SAF Project Team, 2010), and the ‘SAF for Land Surface Analysis (LSA SAF) Validation Report LST’ (Trigo et al., 2009a).

Satellite based remote sensing is the only realistic means by which the land surface can be monitored frequently and on large scales. The last decades have seen a steady increase of space-borne sensors with ever increasing capabilities with respect to spectral, spatial, and temporal resolution, e.g. compared to its predecessor the data volume produced by MSG/SEVIRI has risen from 1 Terabyte to 20 Terabyte per year. This trend is set to continue and many satellite imagers will have hyperspectral rather than multispectral capabilities, i.e. hundreds of spectral channels instead of a few tens. These developments require more automated data processing and algorithms capable of extracting and summarizing the relevant information. Further challenges are posed by analyses of relations between independent space-derived parameters, e.g. LST and vegetation indices, e.g. NDVI, which have to be systematically studied and interpreted in the framework of global change research (Stoll, 1994; Lambin and Ehrlich, 1996). Like NDVI data, LST derived from single observations are usually spatially discontinuous due to cloud cover. Therefore, researchers have investigated applications of temporal composites of LST:

- **Epidemiology:** Neteler (2005) used monthly mean composites of LST derived from MODIS/Terra to extend an epidemiological study about the exposure risk to Lyme and tick-borne encephalitis (TBE). The reasoning behind this application is that the distribution of tick-borne diseases can be related to “autumnal cooling”, an index describing the autumnal temperature decline from August to October (northern hemisphere). Sites of tick-borne encephalitis (TBE) appear to be characterized by a high rate of autumnal cooling, relative to the

annual maximum of the monthly mean LST level in midsummer (Randolph et al., 2000).

- **Land Surface Cover (Change):** In-situ land surface temperatures have limited applications, since many areas are poorly represented or provide no observations. Satellite measurements can fill data voids and help to obtain more complete LST maps. Lambin and Ehrlich (1997) obtained monthly maximum value composites from 20 years of daily NDVI and LST data (NOAA/AVHRR) to perform land-cover change analyses over Africa. Barbosa et al. (1998) investigated the usefulness of various compositing techniques for NDVI and LST, including weekly maximum composites, to detect burned areas in AVHRR-GAC 5km data. Basist et al. (1998) first obtained LST composites from the Special Sensor Microwave/Imager (SSM/I) data and then used the composites to derive snow cover and wetness maps for a 2-week blizzard period. Mildrexler et al. (2007) used annual maximum composite LST data to detect fundamental changes in land-surface energy partitioning, which are indicators for land cover changes due to wildfire, insect epidemics, flooding, climate change and human-triggered land-use. Long-term composites avoid the high natural variability associated with tracking LST at daily, weekly, or seasonal time frames. Roy (1997) investigated the impact of maximum compositing on land cover classification, which he demonstrated with a forest/non-forest classification based on NDVI and LST data derived from AVHRR.
- **Land Surface Evaporation / Drought Detection:** in order to improve the detection of droughts from space, Kogan (1995; 1997) developed a temperature condition index (TCI) based on NOAA/AVHRR brightness temperatures. The TCI complements the vegetation condition index (VCI), a normalised index derived from NDVI that accounts for local differences in vegetation dynamics. In a combined application of VCI and TCI to drought monitoring over India, Singh et al. (2003) found that the two indices complement each other: VCI can detect vegetation stress while TCI indicates whether the stress is due to dryness or excessive wetness. Thus, TCI helps to identify droughts and avoid false alarms. In a more recent study Rojas et al. (2011) successfully combined TCI and VCI to map the risk of drought occurrence over Africa. Partitioning of solar energy at the Earth surface has significant implications in climate dynamics, hydrology, and ecology. Nishida et al. (2003) used NOAA/AVHRR 14-day composites of NDVI and LST to estimate the evaporation fraction of bare soil from “VI-Ts” (vegetation index-surface temperature) diagrams. Sandholt et al. (2002) suggested a simplified land surface dryness index (Temperature–Vegetation Dryness Index, TVDI) based on an empirical parameterisation of the relationship between LST and NDVI. They used NOAA / AVHRR data to estimate the "dry edge" in LST/NDVI space by extracting maximum LST for small Intervals of NDVI. Intermittent coverage makes application of TIR methods in tropical regions quite unreliable and impractical. Using environmental metrics such as LST/NDVI derived from monthly and longer composite AVHRR imagery have provided regional-level information about drought in such cloudy regions (McVicar and Bierwirth, 2001). Cleugh et al. (2007) performed routine monitoring of landscape-scale evaporation; they used 8-day composites of 1 km MODIS LST to estimate evaporation at 16-day

intervals. An overview of methods for estimating land surface evaporation from remotely sensed surface temperature data is given by Kalma et al. (2008).

- **Cloud Detection:** Jedlovec et al. (2008) used 20-day composites of the 11 μ m channel and the 11 μ m –3.9 μ m channel difference of GOES-12 to represent spatially and temporally varying clear-sky thresholds for the bispectral cloud tests. Such dynamically generated thresholds yield significant improvements in cloud detection, particularly during the more difficult night time period. Stöckli (2013) improved the cloud clearing thresholds of ‘The HelioMont Surface Solar Radiation Processing’ by modelling diurnal cycles (Göttsche and Olesen, 2001) of Meteosat LST. Baroncini et al. (2008) used a modified Kalman Filter to obtain a dynamic cloud masking and filtering algorithm based on modelled LST.
- **Harmonic Analysis:** The monitoring of NDVI time series can only evidence the areas having seen increases or decreases in vegetation, while its combined use with LST time series allows determining if the changes affect the seasonal behaviour of the existing vegetation, or if the changes are due to changes in the land cover. Julien et al. (2006) used maximum composites of NDVI and LST (Pathfinder AVHRR Land dataset) as input to HANTS (Harmonic ANalysis of Time Series) software, which allowed them to simultaneously observe the mean value, first harmonic amplitude and the phase behaviours. The analysis was conducted on a yearly basis for series of 36 10-day maximum composite images. Among others, it confirmed a rise in wood proportion in Europe, as well as the desertification of southern areas.

Nearly all of the above applications are based on polar orbiter data: since (earth observation) polar orbiters are usually on sun-synchronous orbits, the corresponding composites represent maximum LST at the *time of observation* (e.g. for the "solar noon" overpass around 13:30h solar time). However, the overall maximum LST generally does not occur at the overpass time. Furthermore, the low temporal resolution of polar orbiters (e.g. 2-4 LST per day) does not allow the recovery of complete diurnal temperature cycles (DTC) of maximum LST, i.e. maximum LST at any time of day. In contrast, the high sampling rate of geostationary satellites, e.g. 15 min for MSG/SEVIRI, allows to accurately determine the time and the value of the overall maximum LST as well as to resolve the temporal dynamics of the composite LST, i.e. entire maximum composite DTC can be extracted and analysed with methods developed for individual (cloud-free) DTC.

In order to study the surface temperature of the Moon, Jaeger (1953) developed a one-dimensional model of heat-conduction with periodic boundary conditions (Carslaw and Jaeger, 1959). The original model was modified for thermal inertia studies of the Earth (Watson, 1973; Price, 1977; Cracknell and Xue, 1996; Liu et al., 2015) and the associated non-linear boundary condition for the energy fluxes at the surface is solved by linearization or numerical (Fourier) analysis (Watson and Hummer-Miller, 1981). By combining a cosine term with an exponential decay function, Göttsche and Olesen (2001) developed a simple physics-based model of cloud-free DTC. Fitting this model to DTC summarizes the thermal behaviour of the land surface and yields sets of representative and informative "Thermal Surface Parameters (TSP)": these can be used to reconstruct the complete diurnal cycle of temperature, including the interpolation of atmospheric corrections and missing LST derived from satellite data (Schädlich et al., 2001; Jiang et al., 2006; Inamdar et al., 2008; Inamdar and French, 2009; Duan et al.,

2012) and for improving cloud screening algorithms (Reuter, 2005; Stöckli, 2013). Göttsche and Olesen (2009) improved their original model by accounting for the effect of total optical thickness (TOT) on DTC. Including TOT as an additional parameter, also potentially benefits the determination of atmospheric dust loads over deserts (Cautenet, et al., 1992; Legrand, et al., 1989, 1992); however, this ability of the DTC model still needs to be investigated. Holmes et al. (2013) used the DTC model of Göttsche and Olesen (2001) to compare timing and amplitudes of maximum LST as described by TIR data, MW data, and a model.

2. Algorithm Overview

Composited diurnal MLST cycles (LSA-003A) and TSP (LSA-003B) are both part of the DLST product. Together the DLST sub-products provide a 10-day synthesis of the LSA SAF MLST product (LSA-001) and spatially smooth fields of maximum and minimum temperature. This is achieved in two steps consisting of the estimation of:

- (i) Maximum and Median LST (LSA-003A) within a compositing period of 10 days, per time-slot, leading to a maximum/median value every 15 minutes
- (ii) Thermal Surface Parameters ‘TSP’ (LSA-003B) that summarize maximum and median diurnal temperature cycles given by the LSA-003A products.

The LSA-003B algorithm performs an effective compression of the 15 minute information (96 values per DTC, as contained in the LSA-003A products), through a small number of 7 (6 independent) parameters, which are easy to interpret. The LSA-003A products are subsets of MLST and serve as inputs to LSA-003B: therefore, the LSA-003A algorithm is described together with the LSA-001 algorithm in the MLST ATBD. The MLST product is estimated from TOA brightness temperatures of SEVIRI split-window channels, centred on 10.8 and 12.0 μm (hereafter IR108 and IR120), respectively (Trigo et al., 2009). MLST are the only required input to the DLST (LSA-003) products. The two DLST sub-products, LSA-003A and LSA-003B, their inputs and some applications are listed in Table 1 and flow diagrams summarising the LSA-003 algorithms are shown in Figure 1.

Table 1 Required inputs and purpose of DLST sub-products LSA-003A and LSA-003B.

Inputs	Algorithm	Output & sample applications
up to 960 MLST (10 days LSA-001)	Maximum Composite (LSA-003A) & TSP (LSA-003B)	96 hottest LST (driest conditions) during the 10 days. The TSP summarize the 96 maximum LST and describe a smooth DTC. Purpose: cloud-detection, determination of the "dry edge" in NDVI-LST space, and for identifying vegetation stress.
	Median Composite (LSA-003A) & TSP (LSA-003B)	96 average LST (most typical conditions) during the 10 days. The TSP summarize the 96 max. LST and describe a smooth DTC. Can be used to define less conservative thresholds for cloud-detection and to improve estimates of minimum temperature.

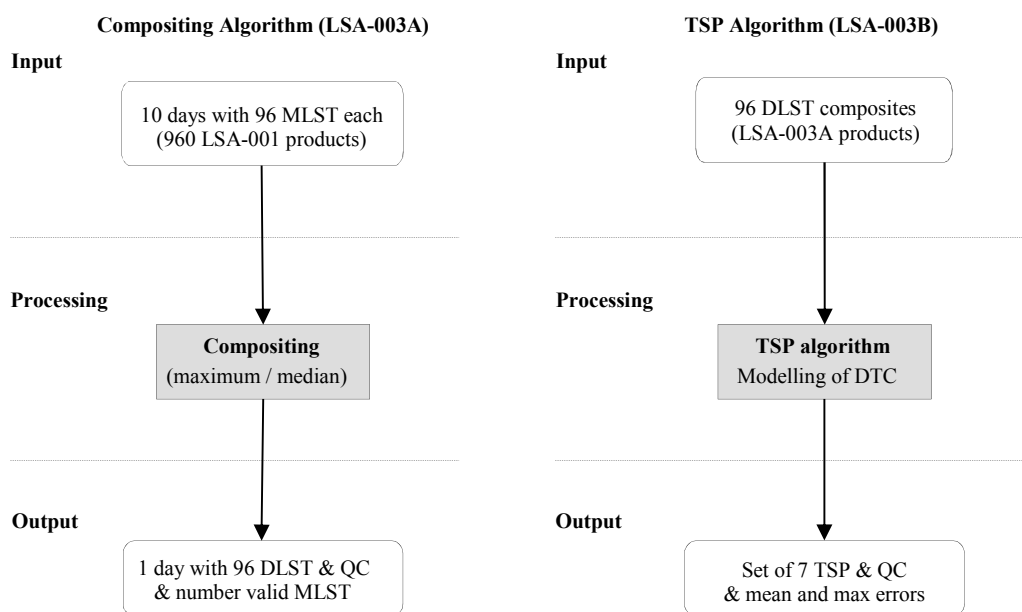


Figure 1 Processing chains of the decadal LST (DLST) algorithms (LSA-003). Left: Temporal LST composites (LSA-003A). Right: Thermal Surface Parameters (TSP) algorithm (LSA-003B). The TSP algorithm fits a model of the diurnal temperature cycle (DTC) to DLST composites. The DTC model and the TSP are explained in Figure 6 and Table 2.

2.1. LST Composites as Input to LSA-003B Algorithm

Modelling composite LST gives spatially continuous fields of TSP and modelled LST, which is advantageous for operational purposes as well as for many applications. The LST composite products are described in the MLST (LSA-001) ATBD and serve here as input to the LSA-003B algorithm. Two temporal (decadal) composites are derived from the MLST product (SEVIRI/Meteosat 15 minute LST): DLST maximum

and median composites (LSA-003A). Maximum composites, i.e. maximum LST per observation time-slot within a 10-day period, are well established and highly popular due to their simplicity (Holben, 1986). However, median composites (median per observation time slot) are computationally only slightly more demanding with the biggest difference being data handling and storage. An advantage of median LST is that they represent the typical situation within the composition interval. In contrast, maximum composites collect the highest observed LST and are, therefore, not necessarily representative. When composites of too few input data are formed (e.g. from 2 valid measurements), they tend to be cloud contaminated. Therefore, the number of measurements used to create a composite should be monitored and should be kept for later interpretation. Minimum LST composites tend to pick up values contaminated by undetected clouds, since these are generally colder than cloud-free pixels: this is the reason why LSA SAF (and other data providers) do not produce minimum composites. However, modelling median LST composites with the DTC model yields good and stable estimates of representative minimum LST within the compositing period.

Figure 2 to Figure 5 show some layers of a LST composite product LSA-003A. When comparing the maximum LST composite in Figure 2 with the median composite in Figure 3, the most obvious features are a) the lower median temperatures and b) the finer and more continuous structures in the median composite, e.g. demonstrated by the Apennines, Italy, and by the Bordeaux area, France (45° N, 0° E). Some hot areas in Algeria (around 60°C) have considerably colder LST in the median composite and show more structure.

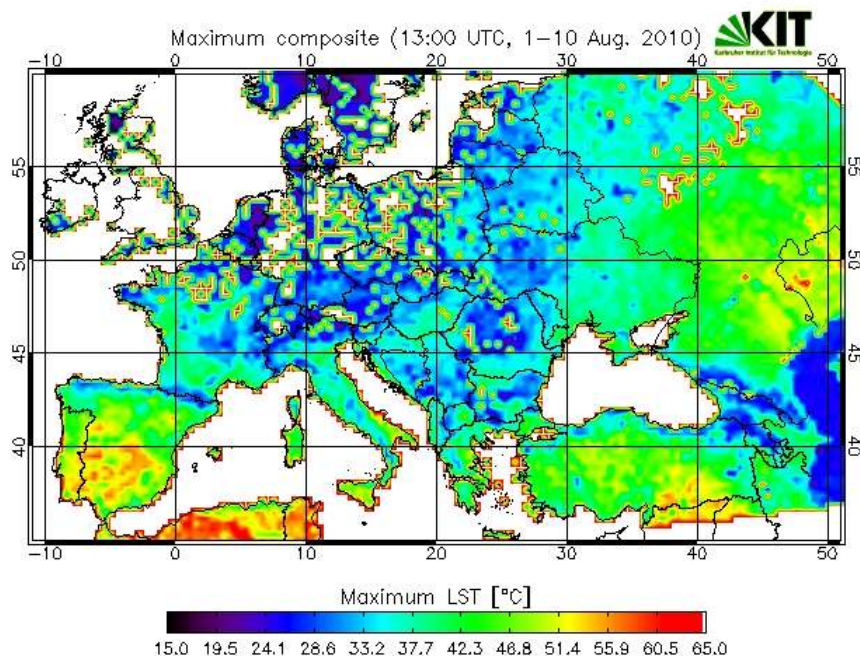


Figure 2 Maximum LST for 13:00h UTC derived from the first 10 days of August 2010.

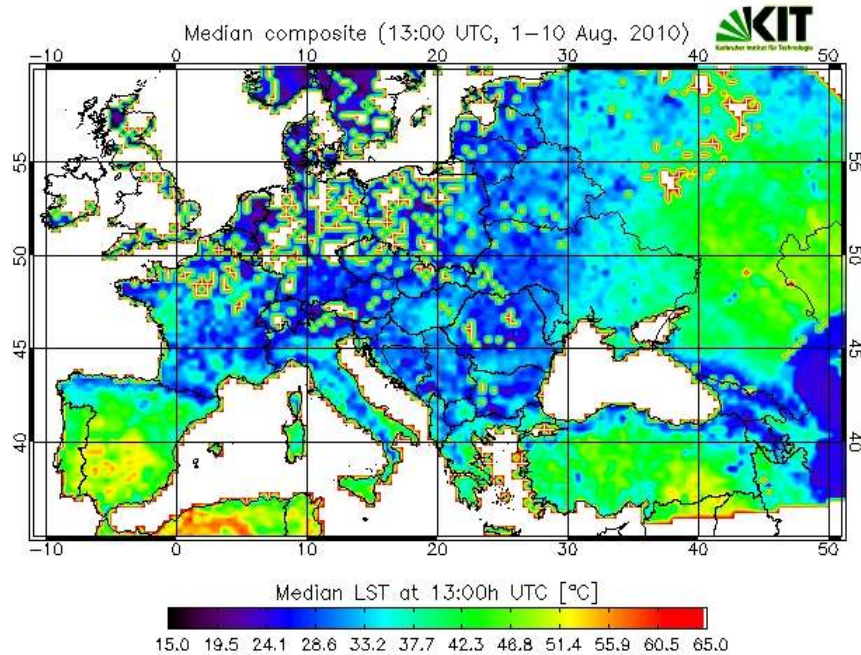


Figure 3 Median LST for 13:00h UTC derived from the first 10 days of August 2010.

Figure 4 shows the number of valid LST found at 13:00h UTC between the 1st and 10th of August 2010 (identical for median and maximum composite). The number of valid LST mainly reflects the cloud situation at the time of acquisition. Figure 5 shows the errors associated with each maximum LST (Figure 2); the errors were taken directly from the respective layer of the input MLST product (LSA-001) and give a good idea about the quality of the LST. Furthermore, the additional product layers allow an identification of areas with unusual behaviour, e.g. in the error bar plot (Figure 5) there is an area with high LST errors (red) in Algeria which at the same time has between 6 to 10 valid LST as input to the composite (Figure 4).

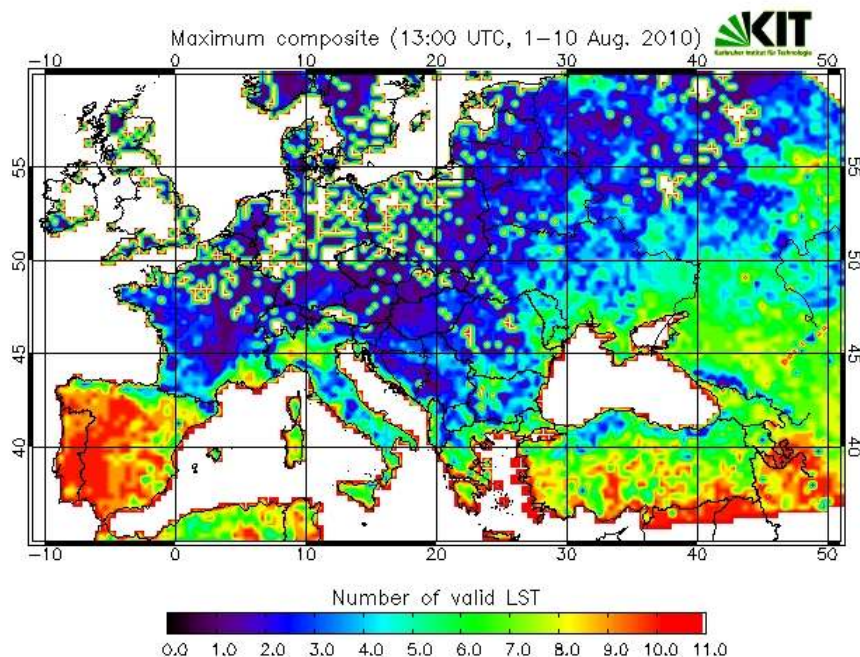


Figure 4 Number of valid LST found at 13:00h UTC during the first 10 days of August 2010.

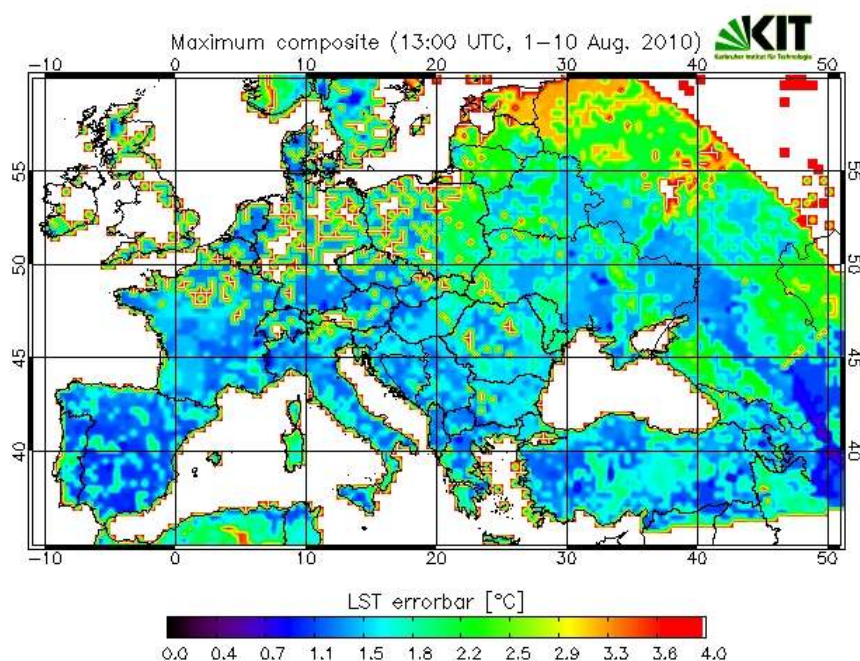


Figure 5 Errors associated with maximum LST at 13:00h UTC for the first 10 days of August 2010.

3. Algorithm Description

In the following, the DTC model of Göttsche and Olesen (2001) is referred to as the “Goe2001” model while the model of (Göttsche and Olesen, 2009), which is also the basis of his ATBD, is referred to as the “Goe2009” model.

3.1. Theoretical Description

3.1.1. Physics of the Problem

Previous work on modelling the DTC of the land surface neglects the effect of the atmosphere on solar irradiation or treats atmospheric transmittance in the visible as constant (Price, 1977; Cracknell and Xue, 1996): it assumes that the half-wave heating flux closely approximates the solar flux for clear sky conditions and can be expressed as a half cosine (Watson and Hummer-Miller, 1981; Cracknell and Xue, 1996; Watson, 1999; Göttsche and Olesen, 2001). However, the transparency of the atmosphere decreases in the presence of aerosols and dust and, consequently, the amount of solar energy reaching the surface and the heating flux are reduced and do not have a pure cosine form (Watson and Hummer-Miller, 1981; Legrand, et al., 1989; Cautenet, et al., 1992; Legrand, et al., 1992). Furthermore, the emitted long-wave radiance of hot surfaces is partially screened by colder dust layers, which results in an apparent cooling effect in satellite observations. At night-time, dust enhances the infrared flux incident at the ground and results in a local greenhouse effect (Tanre and Legrand, 1991). In the following, the Goe2009 model of Göttsche and Olesen (2009) is described, which is based on the energy balance equation at the surface and which accounts for the effect of atmospheric attenuation on extra-terrestrial solar irradiation. The cosine term of the DTC model and its dependence on solar zenith angle follow naturally from the model's dependence on solar irradiation. Radiative cooling at “night-time” is described with an exponential decay term and requires that daytime and night-time parts smoothly fit together at “thermal sunset”, i.e. the model has to be differentiable. The effect of atmospheric attenuation on solar irradiation is accounted for by the model parameter total optical thickness (TOT) – one of the so-called ‘thermal surface parameters’ (TSP) – and leads to a dependence on relative air mass. The model correctly reproduces the slow and smooth increase of LST around sunrise and it has the ability to temporally “squash” modelled DTC to match the shape of the actual DTC (Göttsche and Olesen, 2009; Duan et al., 2012).

The typical shape of the Goe2001 and Goe2009 models is illustrated in Figure 6 and the model parameters are explained in Table 2. In order to reduce the number of independent parameters, Göttsche and Olesen (2001) identified parameter “width ω ” with the daily duration of energy input by the sun, i.e. the hours of daylight. However, the Goe2001 model cannot reproduce the day to day variability in DTCs general shape, i.e. it does not explain the variation in the width of the temperature peak, nor does it reproduce the observed slow and smooth increase of surface temperature at sunrise. Instead of beginning from the equation of thermal diffusion (Carslaw and Jaeger, 1959), the formulation of the Goe2009 model starts from the energy balance equation at the surface. This is motivated by the observation that the so-called “force-restore equation”, which is derived from the equation of thermal diffusion with a single harmonic forcing term, is an approximation of the energy balance equation at the surface (Yee, 1988).

Both models obtain attenuation constant k via the assumption of differentiability at time t_s (Figure 6), when the model's term for 'daytime' ends and 'night-time' starts.

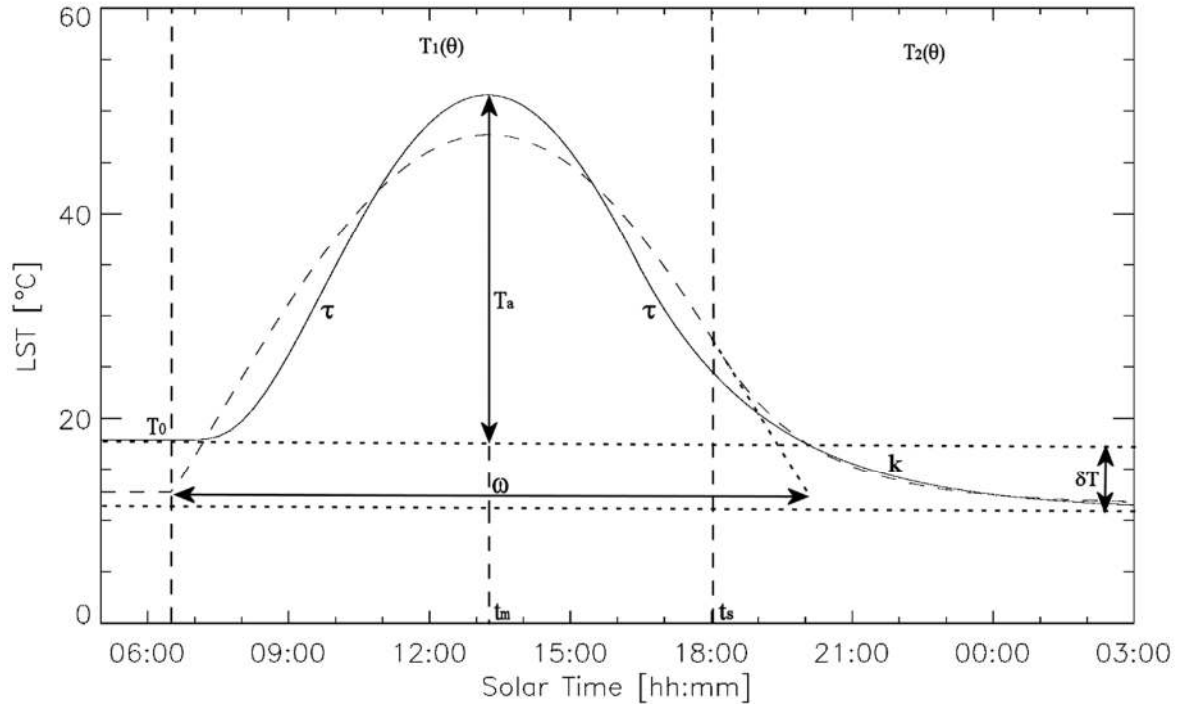


Figure 6 Model parameters (Table 2) and fits of the DTC model “Goe2009” (solid line, eq. (16)) and of the Göttsche and Olesen (2001) model “Goe2001” (broken line) to sample LST (data omitted for clarity). The “daytime” part T_1 (sunrise to start of attenuation function at t_s) and the “night-time” part T_2 (t_s to end, here 03:00h) of the models are indicated by broken vertical lines.

Table 2 Meaning of the model parameters in the Goe2001 and Goe2009 models.

Parameter	Meaning
T_0 [°C]	minimum temperature
T_a [°C]	temperature amplitude ($= T_{\max} - T_0$)
t_m [solar time]	time of the maximum
t_s [solar time]	start of the attenuation function
δT [°C]	$T_0 - T(t \rightarrow \infty)$, where t is time
ω [hh:mm]	half-period of cosine oscillation (Goe2001)
k [hh:mm]	attenuation constant (calculated with eq. (18))
τ	total optical thickness (TOT)

3.1.2. Mathematical Description of the Algorithm

At sun-earth distance, with solar constant $I_0 = 1367 \text{ W/m}^2$ and eccentricity factor e_N , the extraterrestrial irradiance on a plane with sun zenith angle θ_z is (Iqbal, 1983)

$$I_{ext}(\theta_z) = I_0 \cdot e_N \cdot \cos(\theta_z) \quad (1)$$

$$\cos(\theta_z) = \sin(\delta)\sin(\phi) + \cos(\delta)\cos(\phi)\cos(\theta) \quad (2)$$

$$\theta_z = \arccos[\sin(\delta)\sin(\phi) + \cos(\delta)\cos(\phi)\cos(\theta)] \quad (3)$$

Where δ is solar declination, ϕ is the latitude, and $\theta = \varphi \cdot t = \frac{\pi}{12\text{h}} \cdot t$ is the “hour angle”

with respect to solar noon, with angular velocity φ of the earth’s rotation ($\frac{\pi}{12\text{h}}$) and time t ; time and hour angle are zero at solar noon, negative in the morning, and positive in the afternoon. On its path through the atmosphere the extraterrestrial irradiance is partially absorbed and scattered by molecules (Raleigh) and aerosols (Mie). Assuming a plane parallel atmosphere and monochromatic light, the Beer-Lambert law can be used to calculate the direct solar (shortwave) radiation which reaches the earth’s surface:

$$S^\downarrow(\theta_z) = I_{ext} \cdot e^{-\tau \cdot m(\theta_z)} = I_0 \cdot e_N \cdot \cos(\theta_z) \cdot e^{-\tau \cdot m(\theta_z)} \quad (4)$$

Where τ is total optical thickness (TOT), i.e. the attenuation constant for a vertical path through the atmosphere, and θ_z is solar zenith angle calculated via equation 3. Neglecting refraction, relative optical air mass $m(\theta_z)$ can be obtained from the following theoretical or empirical relationships:

$$m_{simple}(\theta_z) = \frac{1}{\cos(\theta_z)} \quad (5)$$

$$m_{kasten1989}(\theta_z) = \frac{1}{\cos(\theta_z) + a \cdot (b - \theta_z)^{-c}} \quad \text{with } \theta_z \text{ in degrees} \quad (6)$$

$$m_{vollmer2006}(\theta_z) = \frac{r(\theta_z)}{H} = -\frac{R_E}{H} \cos(\theta_z) + \sqrt{\left(\frac{R_E}{H} \cos(\theta_z)\right)^2 + 2\frac{R_E}{H} + 1} \quad (7)$$

Where $m_{simple}(\theta_z)$ is the simplest formulation of relative air mass and assumes a plane-parallel homogenous atmosphere. $m_{kasten1989}(\theta_z)$ is an empirical relationship parameterized by Kasten (1989) for the US standard atmosphere. Here, $m_{kasten1989}(\theta_z)$ is formulated for sun zenith angle θ_z ; therefore, the constants are $a = 0.50572$, $b = 96.07995$, and $c = 1.6364$ (Kasten, 1989). Based on geometric considerations, Schoenberg (1929) calculated the path of light through a radially symmetric, homogeneous atmosphere (uniform and constant density), which Vollmer and Gedzelmann (2006) used to define the optical air mass: $m_{vollmer2006}(\theta_z)$ is the ratio between the length of a slanted path $r(\theta_z)$ and the thickness of the atmosphere (“scale

height”) $H = \frac{RT_{atm}}{gM_{mol}}$; with ideal gas constant $R = 8.314472 \text{ JK}^{-1} \text{ mol}^{-1}$, $M_{mol} = 28.97 \text{ gmol}^{-1}$ for dry air, $g = 9.81 \text{ ms}^{-2}$, and $T_{atm} = 288 \text{ K}$ one obtains $H \approx 8430 \text{ m}$. R_E is the radius of the earth (mean $R_E = 6371 \text{ km}$). Air mass $m_{simple}(\theta_z)$ is accurate up to around 30 degrees and – depending on the needed accuracy – yields reasonable values for angles up to 70 degrees, but its limitations are readily seen from $1 \leq m_{simple}(\theta_z) \leq \infty$. In contrast, $m_{kasten1989}(\theta_z)$ and $m_{vollmer2006}(\theta_z)$ vary correctly between 1 and around 38 and are accurate for zenith angles up to around 85 degrees compared to tabulated values for the US standard atmosphere. The operational TSP product (LSA-003B) described in this document uses the air mass definition of Vollmer and Gedzelmann (equation (7)). This is motivated by the fact that this air mass formulation can be adjusted to specific atmospheres (via scale height) and is differentiable at all zenith angles, which is advantageous for numerical stability.

For dry bare soil as in the Gobabeb gravel plain (in-situ validation site, see Göttsche et al. (2013)) the ground heat flux G at day-time is approximately proportional to net radiative flux R_n (Liebethal and Foken, 2007) and Latent heat flux LE is negligible. Sensible heat flux H is assumed to be directly proportional to *shortwave* net radiative flux $S^\downarrow - S^\uparrow$: this is based on the fact that sensible heat flux H is driven by the difference between surface temperature and air temperature, which – at least approximately – follows $S^\downarrow - S^\uparrow$. In the absence of advection of energy, the energy balance then simplifies to:

$$0 = R_n - H - LE - G = S^\downarrow - S^\uparrow + L^\downarrow - L^\uparrow - c_H \cdot (S^\downarrow - S^\uparrow) - c_G \cdot R_n \quad (8)$$

Where c_H is a dimensionless constant linking H to net shortwave flux, c_G is a dimensionless constant linking G to net radiative flux R_n , and S^\uparrow and L^\uparrow are the upwelling and S^\downarrow and L^\downarrow the down-welling shortwave and longwave fluxes, respectively. The assumption of constant c_G is only approximately valid at day-time and c_G depends on soil type and conditions as well as vegetation cover (Kustas and Daughtry, 1990; Bastiaanssen et al., 1998; Liebethal and Foken, 2007). By solving equation 8 for L^\uparrow and applying Stefan-Boltzmann’s law and Kirchhoff’s law we now derive an expression for surface temperature T :

$$L^\uparrow = (S^\downarrow - S^\uparrow) \cdot (1 - c_H) + L^\downarrow - c_G \cdot (S^\downarrow - S^\uparrow + L^\downarrow - L^\uparrow) \quad (9)$$

$$\varepsilon \cdot \sigma \cdot T^4 + L^\downarrow \cdot (1 - \varepsilon) = S^\downarrow \cdot (1 - A) \cdot (1 - c_H - c_G) + L^\downarrow - c_G \cdot [L^\downarrow - \varepsilon \cdot \sigma \cdot T^4 - L^\downarrow \cdot (1 - \varepsilon)] \quad (10)$$

$$(1 - c_g) \cdot \varepsilon \cdot \sigma \cdot T^4 = S^\downarrow \cdot (1 - A) \cdot (1 - c_H - c_G) + L^\downarrow \cdot \varepsilon \cdot (1 - c_G) \quad (11)$$

$$T = \left(\frac{L^\downarrow}{\sigma} + \frac{(1-A) \cdot (1-c_H - c_G)}{(1-c_G) \cdot \sigma \cdot \varepsilon} \cdot S^\downarrow \right)^{\frac{1}{4}} \quad (12)$$

where A is broadband albedo and ε is broadband emissivity of the surface. If we assume A , ε , and L^\downarrow to be constant (at least over a day), i.e. that no rain event or significant change of lower air mass temperature and humidity take place, then equation 12 depends only on S^\downarrow . Even though L^\downarrow is generally not constant (at Gobabeb it oscillated with daily amplitude of around 80 W/m²) it approximately follows S^\downarrow with a time-lag of about an hour. Therefore, most of the errors due to assuming constant L^\downarrow can be compensated by adjusting c_H . Linearizing surface temperature T with a Taylor series around $S^\downarrow = 0$ yields:

$$T(S^\downarrow) \approx T(0) + \frac{dT(0)}{dS^\downarrow} \cdot (S^\downarrow - 0) = \left(\frac{L^\downarrow}{\sigma} \right)^{\frac{1}{4}} + \frac{dT(0)}{dS^\downarrow} \cdot S^\downarrow \quad (13)$$

$$\text{where } \frac{dT(0)}{dS^\downarrow} = \frac{1}{4} \left(\frac{L^\downarrow}{\sigma} \right)^{-\frac{3}{4}} \cdot \frac{(1-A) \cdot (1-c_H - c_G)}{(1-c_G) \cdot \sigma \cdot \varepsilon} = \text{const.}$$

From equation 13 follows that $T(0) = \left(\frac{L^\downarrow}{\sigma} \right)^{\frac{1}{4}}$. However, this temperature will not be observed in reality, because this temperature is only reached after an infinite amount of time passed without changes in downwelling longwave radiation and without insolation. Therefore, we can only assume $T_0 \approx T(0)$. Setting $\kappa = \frac{dT(0)}{dS^\downarrow}$ and inserting equation 4 for solar irradiation into equation 13 then allows the “day-time” part of the new DTC model to be written as

$$T_1(\theta_z) = T_0 + \kappa \cdot S^\downarrow(\theta_z) = T_0 + \kappa \cdot I_0 \cdot e_N \cdot \cos(\theta_z) \cdot e^{-\tau \cdot m(\theta_z)} \quad (14)$$

In other words, κ is the proportionality constant linking the surface’s thermal response to solar irradiation. At hour angle $\theta = 0$ we have minimum zenith angle $\theta_{z,\min} = \arccos[\sin(\delta)\sin(\phi) + \cos(\delta)\cos(\phi)]$ and minimum relative air mass $m_{\min} = m(\theta_{z,\min})$ and LST (equation 14) reaches its maximum T_{\max} . With temperature amplitude $T_a = T_{\max} - T_0$ follows:

$$T_a = \kappa \cdot I_0 \cdot e_N \cdot \cos(\theta_{z,\min}) \cdot e^{-\tau \cdot m_{\min}} \quad (15)$$

Multiplying both sides of equation 15 by $\frac{e^{\tau \cdot m_{\min}}}{\cos(\theta_{z,\min})}$, substituting $\kappa \cdot I_0 \cdot e_N = T_a \cdot \frac{e^{\tau \cdot m_{\min}}}{\cos(\theta_{z,\min})}$ into equation 14, and then writing the second ("night-time") part of the new DTC model in analogy to Göttsche and Olesen (2001) yields:

$$\begin{aligned} T_1(\theta) &= T_0 + T_a \cdot \cos(\theta_z) \cdot \frac{e^{\tau(m_{\min} - m(\theta_z))}}{\cos(\theta_{z,\min})} \quad \left. \vphantom{\frac{e^{\tau(m_{\min} - m(\theta_z))}}{\cos(\theta_{z,\min})}} \right\} \theta < \theta_s \\ T_2(\theta) &= (T_0 + \delta T) + \left[T_a \cdot \cos(\theta_{zs}) \cdot \frac{e^{\tau(m_{\min} - m(\theta_{zs}))}}{\cos(\theta_{z,\min})} - \delta T \right] \cdot e^{\frac{-12h}{\pi k}(\theta - \theta_s)} \quad \left. \vphantom{\frac{-12h}{\pi k}(\theta - \theta_s)} \right\} \theta \geq \theta_s \end{aligned} \quad (16)$$

The meaning of the parameters in equation 16 is explained in Table 2 and Figure 6. Here, $\theta = \frac{\pi}{12h} \cdot (t - t_m)$ is the “thermal” hour angle with respect to thermal noon at time t_m , which equals solar zenith angle plus some phase shift (time lag between maximum solar irradiation and maximum LST). Similarly, $\theta_s = \frac{\pi}{12h} \cdot (t_s - t_m)$ is the thermal hour angle when the exponential decay part T_2 starts at time t_s and θ_{zs} is the corresponding thermal zenith angle, which is obtained by inserting the thermal hour angles into equation 3. One of equations 5-7 for relative optical air mass $m(\theta_z)$ is inserted into equation 16. A total optical thickness (TOT) $\tau > 0$ in equation 4 reduces solar irradiation and makes the irradiance peak narrower (“squashes it” around solar noon); via equations 16 it has the same effect on modelled DTC around thermal noon. Furthermore, $\tau > 0$ reproduces the observed smooth and gradual (inverse exponential) increase of solar irradiation and LST at sunrise and yields more realistic minimum temperatures T_0 (see Figure 6) for a comparison of the Goe2001 and Goe2009 models).

Continuity of First Derivatives

In order to account for the observed ‘smoothness’ of undisturbed (cloud free) DTCs, the model is required to be differentiable everywhere, also at time $t = t_s$ (at hour angle $\theta = \theta_s$). Applying the chain rule, the first derivatives with respect to time t of the two parts of the model given by equation 16 are:

$$\begin{aligned} \frac{dT_1}{dt} &= \frac{dT_1}{d\theta_z} \cdot \frac{d\theta_z}{d\theta} \cdot \frac{d\theta}{dt} = -T_a \cdot \frac{e^{\tau(m_{\min} - m(\theta_z))}}{\cos(\theta_{z,\min})} \cdot \left[\sin(\theta_z) + \tau \cdot \cos(\theta_z) \cdot \frac{\partial m(\theta_z)}{\partial \theta_z} \right] \cdot \frac{d\theta_z}{d\theta} \cdot \frac{d\theta}{dt} \quad \left. \vphantom{\frac{d\theta_z}{d\theta} \cdot \frac{d\theta}{dt}} \right\} \\ \frac{dT_2}{dt} &= \frac{dT_2}{d\theta} \cdot \frac{d\theta}{dt} = -\frac{12h}{\pi k} \cdot \left[T_a \cdot \cos(\theta_{zs}) \cdot \frac{e^{\tau(m_{\min} - m(\theta_{zs}))}}{\cos(\theta_{z,\min})} - \delta T \right] \cdot e^{\frac{-12h}{\pi k}(\theta - \theta_s)} \cdot \frac{d\theta}{dt} \quad \left. \vphantom{\frac{d\theta}{dt}} \right\} \end{aligned} \quad (17)$$

And therefore the derivatives at $\theta = \theta_s$ must be equal: $\frac{dT_1(\theta_s)}{dt} = \frac{dT_2(\theta_s)}{dt}$.

Cancelling the terms $\frac{d\theta}{dt}$ and solving for k yields:

$$k = \frac{12h}{\pi \cdot \frac{d\theta_z(\theta_s)}{d\theta}} \cdot \frac{\cos(\theta_{zs}) - \frac{\delta T}{T_a} \cdot \frac{\cos(\theta_{z,\min})}{e^{\tau(m_{\min} - m(\theta_{zs}))}}}{\sin(\theta_{zs}) + \tau \cdot \cos(\theta_{zs}) \cdot \frac{\partial m(\theta_{zs})}{\partial \theta_z}} \quad (18)$$

where the $\frac{d\theta_z(\theta_s)}{d\theta}$ is the derivative of zenith angle θ_z (equation 3) w.r.t. hour angle at θ_s ,

$$\frac{d\theta_z}{d\theta} = \frac{\sin(\theta) \cdot \cos(\delta) \cdot \cos(\phi)}{\sin(\delta) \cdot \sin(\phi) + \cos(\delta) \cdot \cos(\phi) \cdot \sin(\theta)} \quad (19)$$

and $\frac{\partial m(\theta_{zs})}{\partial \theta_z}$ is here the derivative of the Vollmer and Gedzelmann (2006) air mass (eq. (7) w.r.t. zenith angle at θ_{zs} :

$$\frac{\partial m_{\text{vollmer2006}}(\theta_z)}{\partial \theta_z} = \frac{R_E}{H} \sin(\theta_z) \cdot \left(1 - \frac{\frac{R_E}{H} \cos(\theta_z)}{\sqrt{\left(\frac{R_E}{H} \cos(\theta_z)\right)^2 + 2\frac{R_E}{H} + 1}} \right) \quad (20)$$

The term $\frac{\delta T}{T_a} \cdot \frac{\cos(\theta_{z,\min})}{e^{\tau(m_{\min} - m(\theta_{zs}))}}$ in equation 18 corrects the attenuation constant k for

changes of the minimum temperature T_0 , e.g. its increase or decrease for days with net gain or loss of heat, respectively. For a completely transparent atmosphere (optical thickness $\tau = 0$) equations 16 and 18 have the same form as the Goe2001 model (Göttsche and Olesen, 2001) but with the additional scaling term $1/\cos(\theta_{z,\min})$. The Goe2009 model contains one more parameter (total optical thickness τ) than the Goe2001 model, but since it does not use width ω as a free parameter, the total number of free parameters is still six. The DTC model given by equations 16 and 18 is non-linear, which means that the corresponding normal equations cannot be solved explicitly. Therefore, a Levenberg-Marquardt scheme (Press et al., 1990) is utilised to fit the model to time-series of LST, e.g. derived from in-situ radiance measurements or taken from the LSA-SAF operational LST product.

3.1.3. Error Budget Estimates

Since the median and maximum composites (LSA-003A) are directly obtained from MLST (LSA-001), these products share the same accuracy requirements, i.e. 4K (threshold), 2K (target) and 1K (optimal); the MLST uncertainty budget is described in detail by Freitas et al. (2010). The uncertainties provided in LSA-003A are copies of the uncertainties provided in the input MLST product (LSA-001). However, during the compositing period usually some data are missing (e.g. due to clouds) and fewer than 10 valid MLST are available per pixel and slot (one of SEVIRI's 96 acquisition times). Since the composites are directly obtained from MLST, they are also subject to uncertainty from undetected clouds. From the above follows, that individual composite LST (LSA-003A) can deviate considerably from their expected values, i.e. those one would obtain by temporally interpolating between the neighbouring composite LST.

The TSP algorithm (LSA-003B) fits a model of the diurnal temperature cycle (DTC) to the entire time series of composite LST (LSA-003A), i.e. it smoothes and temporally interpolates the input composite LST, which considerably reduces the impact of outliers, e.g. due to cloud contamination. The TSP (LSA-003B) have different physical units (time, temperature, unit-less) and, therefore, do not share the MLST product's accuracy requirements. However, there is a correspondence between the LSA-003B layers 'mean_err' and 'max_err' and the LSA-001 product accuracy requirements since the two errors give the average and maximum deviation between the input LST (composites) and the corresponding modelled LST. Assuming that the model describes the DTC of the land surface perfectly and the input data are cloud-free, the deviations between input LST and modelled LST are expected to be random. Under those conditions the average of these deviations would also be subject to the LSA-001 product accuracy requirements (Freitas et al., 2010). Assuming random deviations around the modelled DTC and LST composites (LSA-003A) sharing LSA-001 accuracy requirements, the requirements on the 'mean fit error' of the TSP (LSA-003B) product are set to 2 K threshold, 1.0 K target, and 0.5 K optimal. The latter is in agreement with the findings of Duan et al. (2012), who determined an overall RMSE of 0.4 K when evaluating the Goe2009 model against DTC described by selected days of MSG-SEVIRI LST and in-situ LST.

In-situ measurements show that after short-term cloud cover LST generally returns quickly to clear-sky values (Göttsche et al., 2013). Göttsche and Olesen (2001) studied the effect of 3 h data gaps at various times of the day on derived TSP and obtained a maximum difference of 0.6 K between LST modelled with and without gaps. Stöckli (2013) allowed data gaps of up to 7h (28 SEVIRI slots) when using the Goe2009 model for cloud screening.

3.2. Practical Considerations

Parameter Initialisation

The choice of initial parameter values is usually uncritical: width ω is not needed by the Goe2009 model since the duration of daylight is intrinsically included via zenith angle (equation (3)). Attenuation constant k (equation 18) is calculated once per iteration of the Levenberg-Marquardt minimisation scheme, which simultaneously fits equations 16

to the data. T_o and T_a are initialised based on the maximum and minimum of the DTC. The other parameters are set to reasonable values, e.g. $\delta T = 0.5^\circ\text{C}$ and t_m and t_s are set to 12:30h and 17:00h solar time, respectively. Atmospheric optical thickness is initialised with a representative value for “clear” atmospheres, e.g. $\tau = 0.03$.

3.2.1. Validation and Algorithm Performance

The analysis of the TSP algorithm’s performance presented here has been adapted from the paper by Göttsche and Olesen (2009). The results were obtained by applying the TSP algorithm to nearly cloud-free diurnal cycles of in-situ LST obtained from validation stations at Gobabeb, Namibia and Evora, Portugal. In order to compare the Goe2009 model with Vollmer airmass (eq. (7)) to the Goe2001 model, both models were fitted to LST time series of 54 days and 100 days for Gobabeb and Evora validation sites, respectively. The time series are from periods with low cloud frequency and no additional cloud-masking was performed. The mean fit error (in-situ LST minus modelled LST) at 15 minutes interval for 54 days from Gobabeb is shown in Figure 7, i.e. each data point represents the mean of 54 individual fit errors obtained at the corresponding solar time.

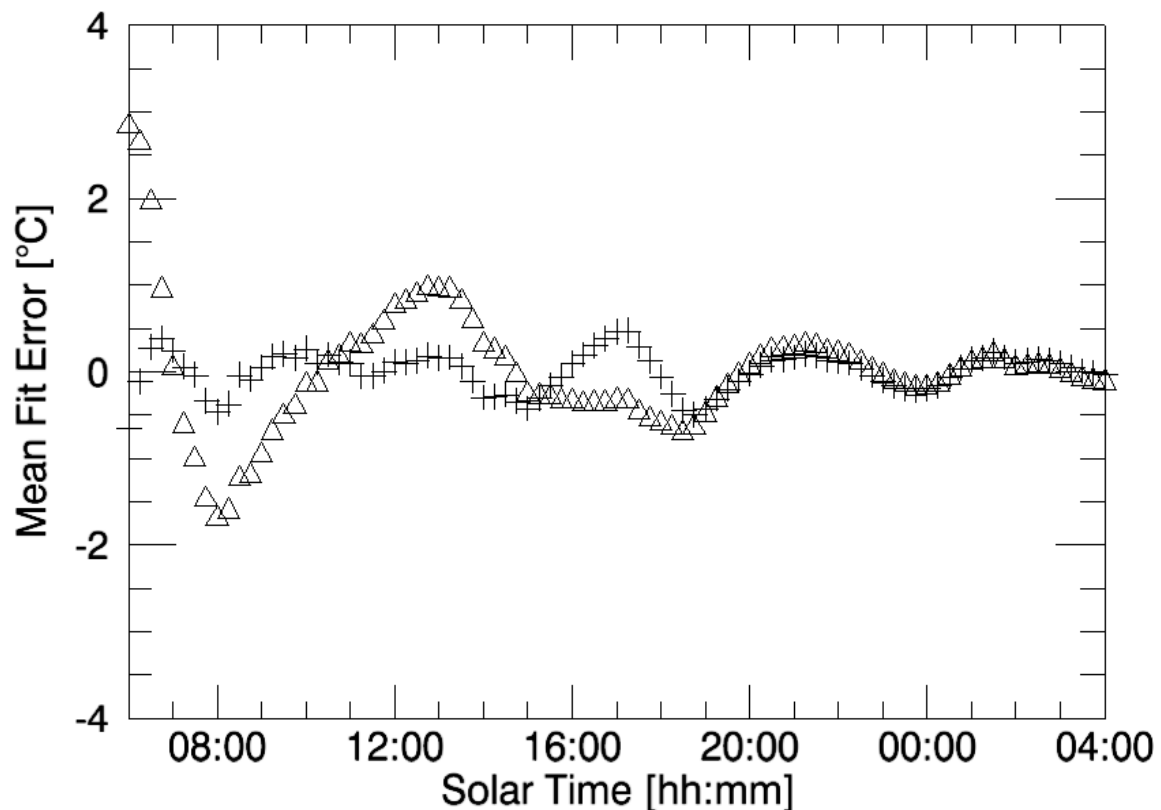


Figure 7 Mean error at 15min interval over 54 days between LST derived from KT-15 East and fitted LST for Goe2001 (triangles) and Goe2009 with Vollmer airmass definition (crosses) at Gobabeb (05.12.2007 to 28.01.2008).

Figure 7 shows that, on average, the Goe2001 model substantially underestimates the measured DTC around sunrise (at about 6h) by 2.8°C and continues to either overestimate or underestimate the DTC until the afternoon, e.g. by 1.0°C around 13h. The considerably smaller values of the mean fit error of the Goe2009

model demonstrate its improved ability to reproduce the DTC. However, in the late afternoon the mean fit error oscillates with amplitude of about 0.5°C , which suggests a relatively small, but systematic mismatch between model and measurements at this time of the day. At night time the two models show small and similar errors of less than 0.5°C .

The effect of different air mass definitions on DTC modelling is shown in Figure 8, which compares the mean fit error of the Goe2009 model for the definitions given by equations (5) - (7). The three definitions result in nearly identical mean fit errors (about 0.5°C). However, the Vollmer air mass performs has the additional advantage of being a) continuous at $\theta_z = 90^{\circ}$ and b) independent of tabulated values for a specific atmosphere.

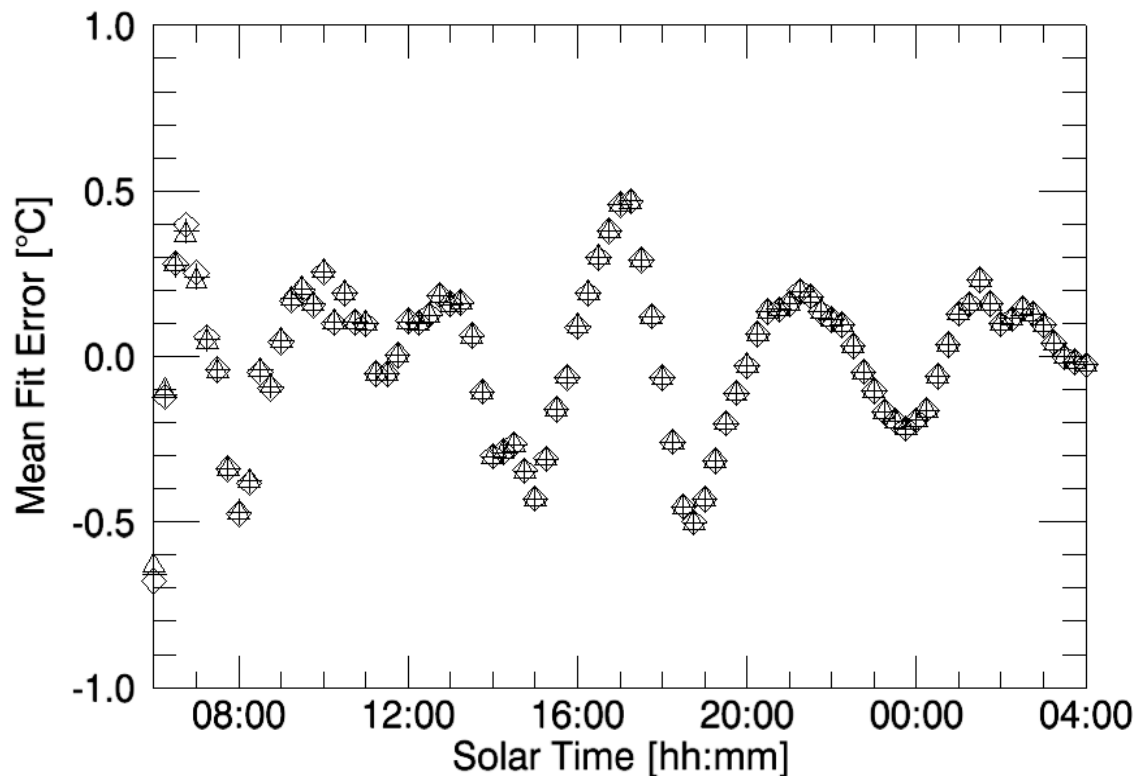


Figure 8 Mean error at 15min interval over 54 days between LST derived from KT-15 East and fitted LST for Goe2009 with airmass definitions according to Vollmer (crosses), simple (diamonds), and Kasten1989 (triangles) at Gobabeb, Namibia (05.12.2007 to 28.01.2008).

The histogram of daily mean absolute deviation of the Goe2009 model from measured LST is shown in Figure 9. The histogram represents the same 54 days used in Figure 7 and Figure 8. The histogram mean is 0.62°C and only 2 days deviate by more than 1°C (Figure 9); bias is minimised by the fitting process and is practically zero. Furthermore, the histogram seems to indicate a bi-modal distribution with one peak near 0.5°C and a second one near 0.8°C : this could be interpreted as overlapping distributions for clear-sky DTC and for DTC with regular disturbances (e.g. fog).

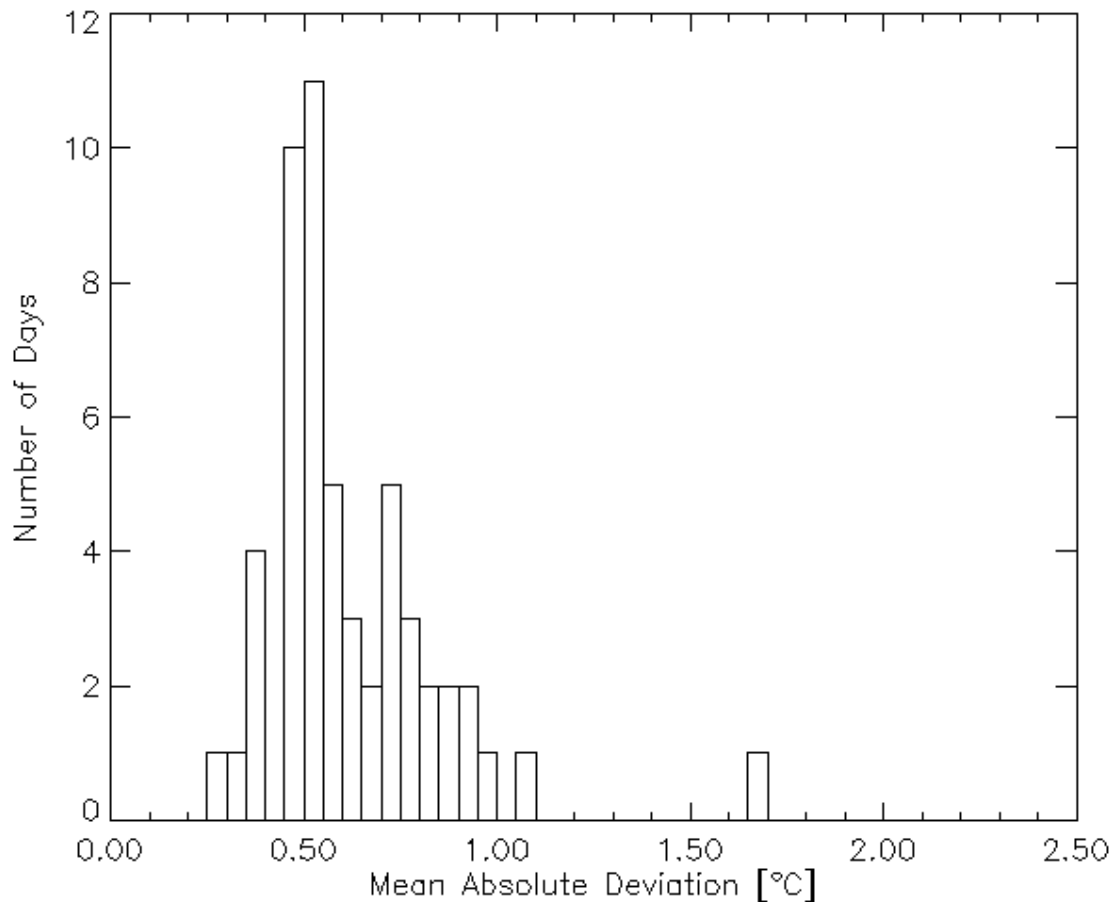


Figure 9 Histogram of mean absolute deviation per day for Goe2009 with Vollmer airmass definition fitted to 54 diurnal temperature cycles measured at Gobabeb, Namibia.

Additionally, the performance of the model is investigated using DTC measured over a grass surface (emissivity set to 0.98) and mid-latitude atmospheric situations (Evora validation site, Portugal see Kabsch et al. (2008)). Figure 10 and Figure 11 show results for measurements taken at Evora validation site in Portugal. The mean fit error (measured LST – modelled LST) for 100 days at 15 minutes interval for Evora is shown in Figure 10. The mean fit error for Goe2001 reaches up to 3.1°C around sunrise and up to -2.8°C around 17 hours. The mean fit error for Goe2009 reaches up to -1.8K around 17 hours. Both models have positive mean errors around 16 hours and negative mean errors around 17 hours, i.e. on average they first underestimate and then overestimate DTC. However, the mean fit error of the Goe2009 model stays below 2.0°C at any time of the day. At night time both models perform similarly.

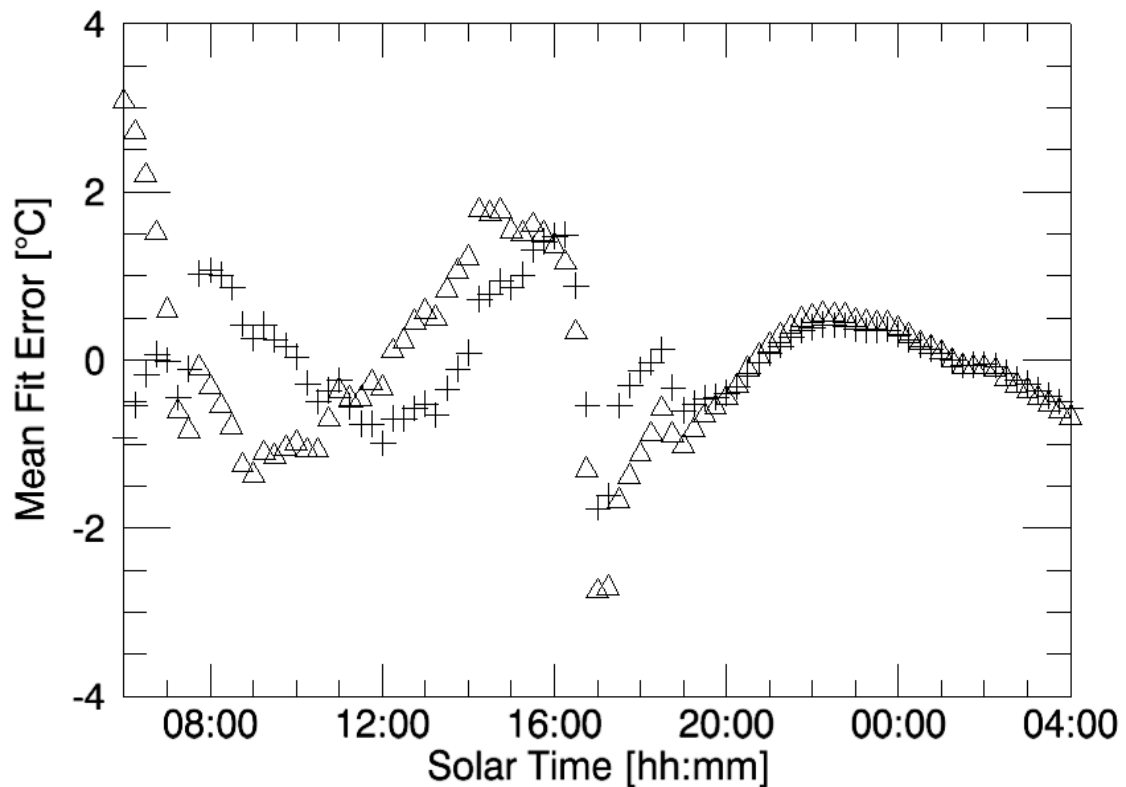


Figure 10 Mean error at 15min interval over 100 days between KT-15 LST and fitted LST for Goe2001 (triangles) and Goe2009 with Vollmer airmass definition (crosses) at Evora, Portugal (11.06.2008 to 08.11.2008).

Figure 11 shows a histogram of daily mean absolute deviation of measured LST from modelled LST for Goe2009. The histogram represents the same 100 days used in Figure 10. The mean of the histogram is 0.97°C and the distribution appears to be uni-modal with its peak near 0.8°C .

The results in this section demonstrate the performance of the algorithm when applied to near-perfect but measured DTC, here represented by time series of in-situ LST from the two validation stations Evora and Gobabeb. The model has shown to describe the general shape of cloud-free DTC well: the average of daily mean absolute deviation between modelled and measured DTC is 0.62°C for Gobabeb and 0.97°C for Evora, where the latter is more effected by cloud-contaminated LST. The histograms for 'mean absolute deviation' per day, e.g. Figure 9, give an impression of the typical accuracy that can be expected for high-quality input data (cloud-free and continuous).

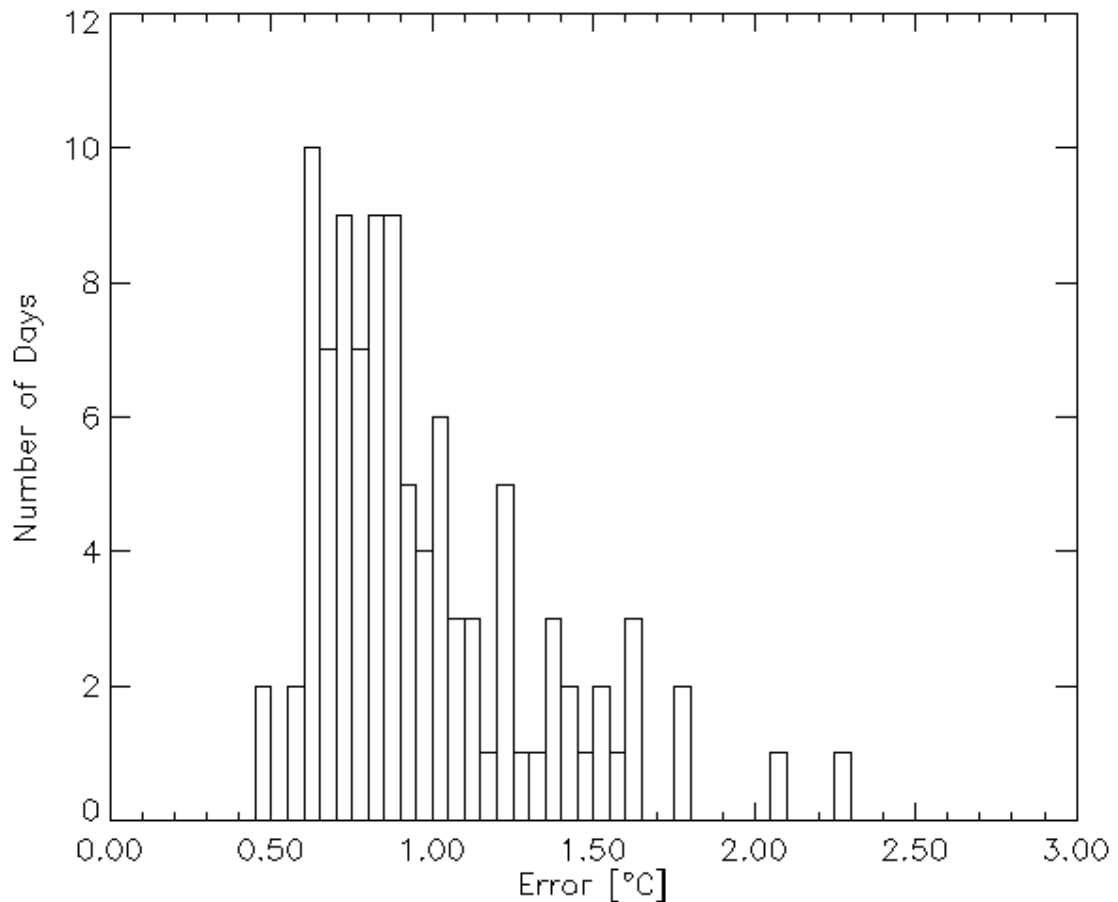


Figure 11 Histogram of mean absolute deviation per day for Goe2009 with Vollmer airmass definition fitted to 100 diurnal temperature cycles measured at Evora, Portugal.

TSP From Decadal LST Composites

The default mode of the TSP (LSA-003B) algorithm uses LSA-003A products (10-day temporal composites of MLST) as inputs; therefore, the LSA-003A algorithm is described in the MLST (LSA-001) ATBD. The input LST composites (LSA-003A) are treated as "normal" MLST slots that describe a synthetic DTC which matches the compositing criterion (i.e. median or maximum). The obtained TSP consist of six independent parameters per pixel and compositing period (see Table 2). Figure 12 to Figure 15 show examples for TSP derived for median composites of MLST. A major advantage of using TSP is that the parameter fields are spatially more continuous than individual MLST (LSA-001) and DLST composites (LSA-003A), which is demonstrated by the few missing data (white areas). The TSP also allow to obtain modelled "maximum composites" (Figure 12) and "minimum composites" (Figure 13), and temperature amplitudes (Figure 14). In contrast to amplitudes directly obtained from DTC data or DTC composites these are generally unaffected by noisy minimum temperatures, which tend to be cloud-contaminated. However, there is significantly more visible detail in the temperature amplitudes than in the maximum temperatures. This can be explained by differences in elevation, thermal inertia, and soil moisture / evapotranspiration, which affect the diurnal range of LST more strongly.

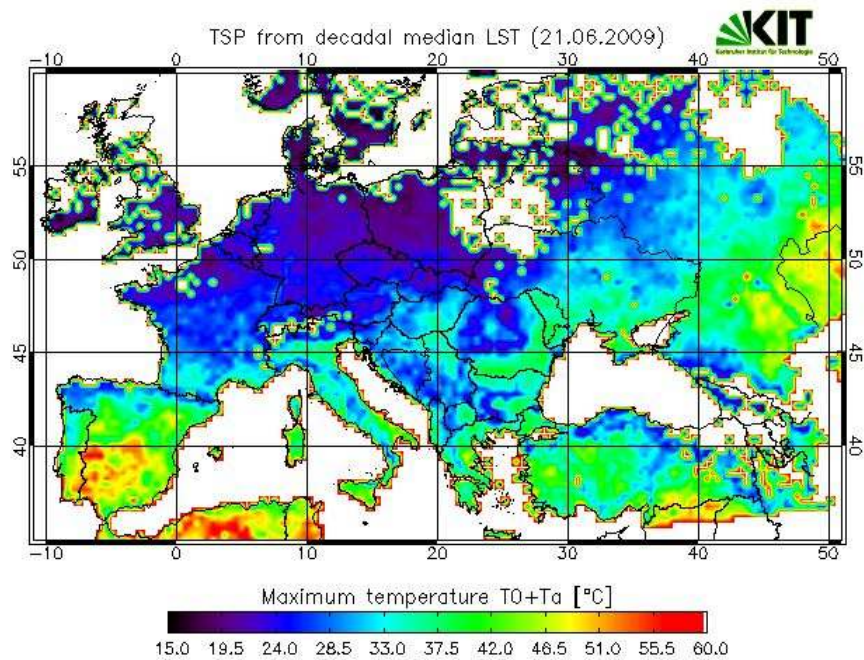


Figure 12 Modelled maximum LST for median DTC of the last 10 days in June 2009.

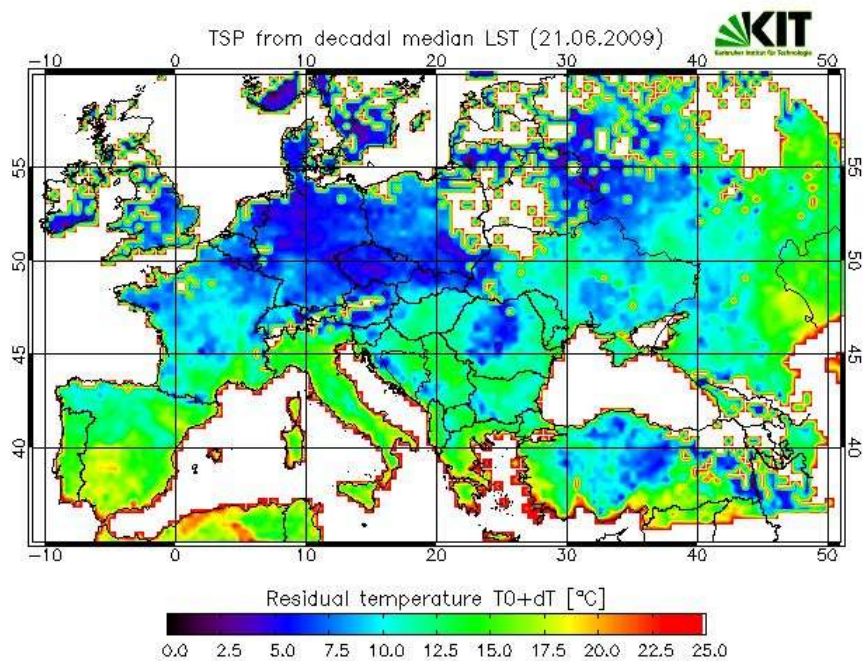


Figure 13 Modelled minimum LST for median DTC of the last 10 days in June 2009.

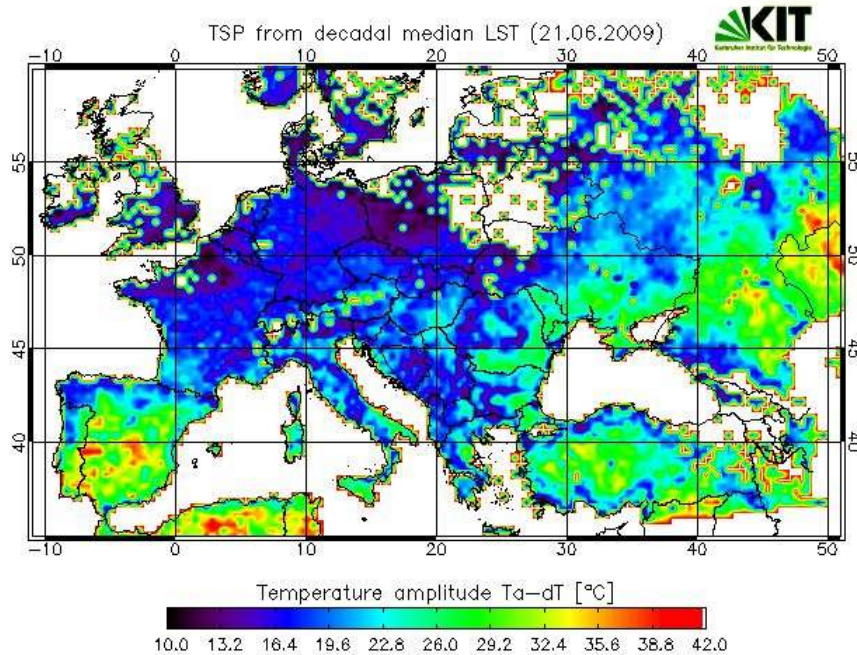


Figure 14 Modelled LST amplitude for median DTC of the last 10 days in June 2009.

Figure 15 shows the time of modelled maximum LST, where time UTC is given in SEVIRI slots, i.e. each slot corresponds to 15 min and slot 49 is 12:00h UTC (alternatively the output can be set to solar time). The figure highlights the impact of solar noon, i.e. the time of maximum LST shifts to progressively later times when moving from east to west. When limiting comparisons to smaller geographical areas, relative differences in the time of maximum LST indicate differences of thermal inertia and local atmosphere, e.g. in Figure 15 North Africa and Italy appear nearly without structure, whereas areas with delayed times of maximum LST are visible in Portugal, parts of Spain and southern France. There are also some areas in Austria with maximum temperatures occurring earlier than in their surroundings: these may be linked to a lake area and to topographical effects. In contrast, the temperature amplitudes (Figure 14) show spatially contrasting features in northern Africa (Algeria; high amplitudes over bare mountain areas) and in Italy (Apennines; low amplitudes over forests). The availability of spatially continuous TSP allows systematic studies of relationships between thermal and other surface parameters, e.g. vegetation indices and surface moisture.

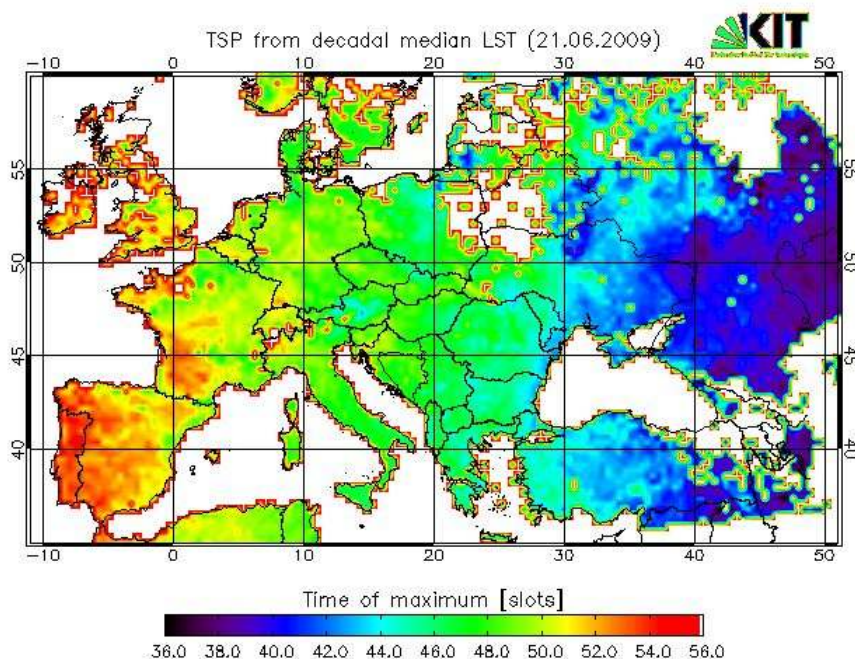


Figure 15 Modelled time of LST maximum for median DTC of the last 10 days in June 2009.

Figure 16 shows the median LST composite at 10:15 UTC for the LSA-SAF geographical region ‘Southern Africa’ over the compositing period 1-10 October 2009. Figure 17 shows the maximum temperatures for the same period, which were determined by fitting the DTC model to the corresponding sequence of median LST composites. In the northern half of the ‘Southern Africa’ region the modelled maximum temperatures have considerably fewer missing values (dark blue pixel) and are less noisy than the LST in the individual median composite shown in Figure 16. The modelled maximum temperatures are less affected by clouds and areas with similar maximum temperatures are spatially more continuous with better defined boundaries. Figure 18 shows the corresponding modelled minimum temperatures and Figure 19 shows the difference between Figure 17 and Figure 18, i.e. the temperature amplitudes. Once re-processed MLST (LSA-001) data are available the TSP (LSA-003B) can be used to derive reliable and smooth TCI, as defined by Kogan (1995).

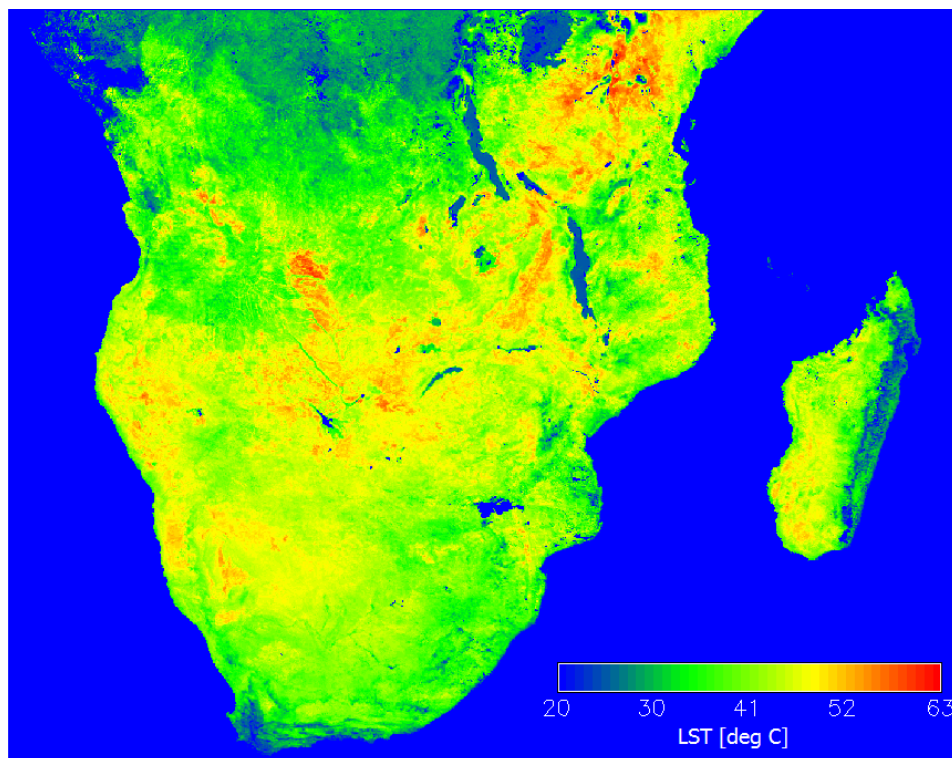


Figure 16 Median LST composite at 10:15 UTC obtained for 1-10 October 2009.

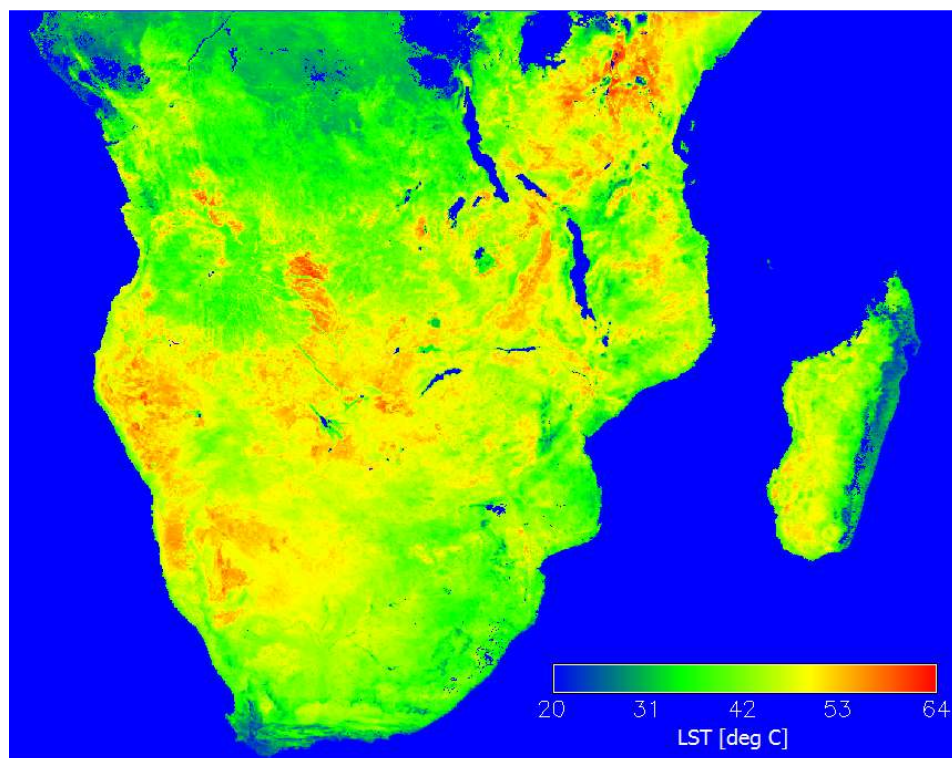


Figure 17 Maximum temperatures Tmax obtained from median DTC for 1-10 October 2009.

High values (red) of minimum temperature (Figure 18) are mainly associated with surface water, whereas the low minimum temperatures are often related to high altitude areas, e.g. the 'blue band' across South Africa occurs over mountains with heights up to 2500 m.

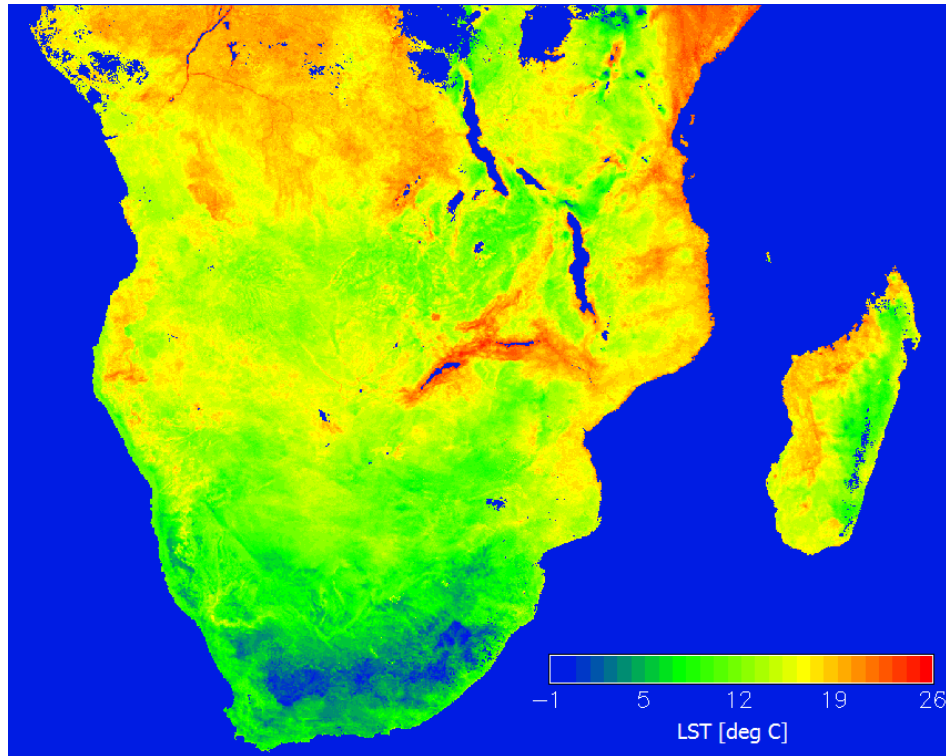


Figure 18 Minimum temperatures T0 obtained from median DTC for 1-10 October 2009.

In contrast, high temperature amplitudes (Figure 19) are usually associated with dry bare surfaces, little evapotranspiration, and low thermal inertia. Most striking in this respect are the high amplitudes over the Namib sand sea and some regions east of it: the Namib consists of high sand dunes (up to 300m) whereas the eastern high amplitude regions (e.g. over the Nama – Karoo Basin and the Kalahari Sandveld) are covered by relatively sparse and usually dry vegetation. These features are shown in more detail in Figure 20, a subset of Figure 19 with a corresponding Landsat 'true colour' image. There clearly is a strong correlation between high amplitudes and major geological features: a result to be expected since there is a close relationship between temperature amplitude and thermal inertia. In contrast, over green vegetation and water bodies, e.g. over the Okavango delta and along the north-eastern edge of the Etosha pan (a large mineral pan into which several perennial rivers drain from North), temperature amplitudes are considerably lower (green-blue areas) due to evapotranspiration and the high thermal inertia of water.

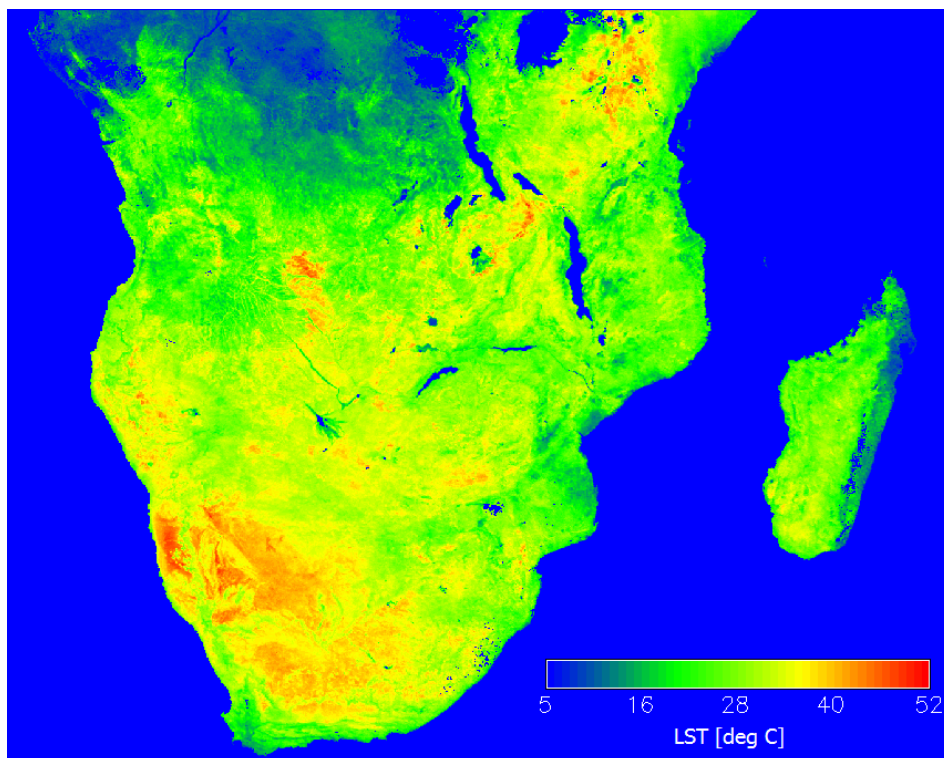


Figure 19 Temperature amplitudes ($T_{max} - T_0$) obtained from median DTC for 1-10 October 2009.

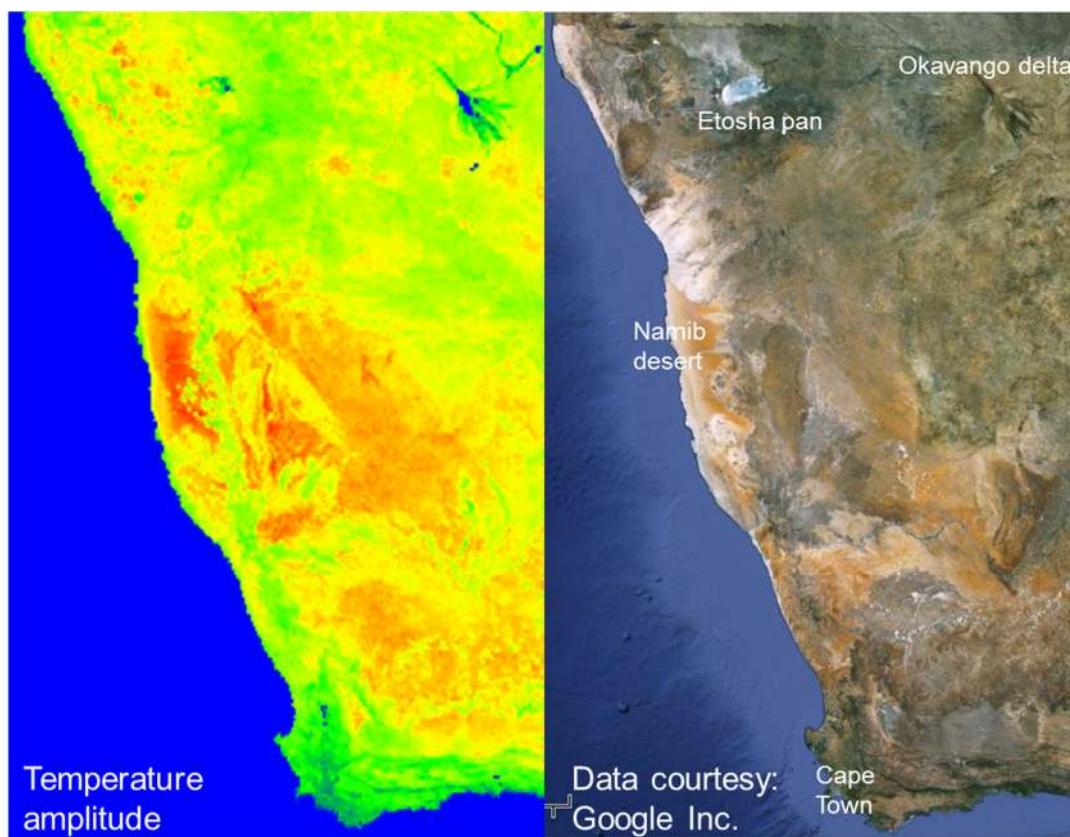


Figure 20 Subset of Figure 19 showing parts South Africa & Namibia (left) and corresponding Landsat ‘true colour image’ (right).

3.2.2. Quality Control & Diagnostics

The quality control (QC) flags listed in Table 3 are contained in dataset ‘qual’ of the HDF5 output file (Table 4). Only for QC = 0 the required constraints on the input LST (e.g. maximum allowed data gap) have been fulfilled; for QC = 64 (maximum number of iterations reached) the results should be treated with care. The dataset ‘mean_err’ (Table 4) should be interpreted against the product’s accuracy requirements, i.e. 2 K threshold, 1.0 K target, and 0.5 K optimal accuracy. Unusually large ‘max_err’ (Table 4) indicate outliers.

Table 3 - Description of DLST TSP (LSA-003B) QC information (flags are additive).

Binary Value	Decimal Value	Description
00000000	0	Result OK
00000001	1	No result: data unevenly distributed
00000010	2	No result: diurnal LST variation too small
00000100	4	No result: data gap too large
00001000	8	No result: too few data points
01000000	64	Warning: maximum number of iterations (10)
10000000	128	Invalid: singular matrix error

3.2.3. Exception Handling

All exceptions are interpreted as ‘singular matrix error’ (QC flag set to 128; Table 3): these usually occur for input data with shapes strongly deviating from clear-sky DTC. After an exception occurred the processing continues with the next pixel location.

3.2.4. Outputs

LSA SAF’s operational processing chain generates TSP (LSA-003B) for inputs of maximum and median decadal LST composites (LSA-003A). The TSP can be regarded as composite data and provide users with the following 10 data fields:

- minimum temperature (approximately at sunrise)
- temperature amplitude
- attenuation constant of exponential decay function
- minimum temperature (model temperature after infinite decay)
- maximum deviation between model and data
- mean deviation between model and data
- quality control information for each model fit
- starting time of the exponential temperature decay
- time of maximum temperature
- total optical thickness of the atmosphere

Table 4 describes the contents of TSP product files (LSA-003B) in more detail.

Table 4 - Contents of the DLST TSP (LSA-003B) product file.

Parameter	Dataset Name	Unit	Range	Variable Type	Scale Factor
Minimum Temperature	T0	°C	[-80, +70]	16-bit Integer	100
Temperature Amplitude	Ta	°C	[+5, +50]	16-bit Integer	100
Attenuation constant	att	15 min , SEVIRI slot	[+0.5, +60]	16-bit Integer	100
Temperature Difference	dT	°C	[-150, +150] Typical: [-10, +10]	16-bit Integer	100
Maximum error	max_err	°C	[0, +70] Typical: [0, +20]	16-bit Integer	100
Mean error	mean_err	°C	[0, +70] Typical: [0, +5]	16-bit Integer	100
Quality Flag	qual	1	[0,192]	16-bit Integer	1
Start time of exponential decay (night)	tdec	15 min , SEVIRI slot	[>= 1] Typical: [50,90]	16-bit Integer	100
Time of maximum temperature	tmax	15 min , SEVIRI slot	[>=1] Typical: [30, 70]	16-bit Integer	100
Total optical thickness	tot	1	[0.01,2.0]	16-bit Integer	10000

4. Assumptions and Limitations

4.1. Assumptions

The DTC model of Göttsche et al. (2009) makes the following basic assumptions:

- 1) only one sunrise takes place (i.e. single DTC are modelled)
- 2) free decay of temperature after “thermal sunset” at time t_s
- 3) clear-sky conditions & no significant changes of surface or atmosphere

The first two assumptions imply that the input data need to be limited to the interval between two consecutive sunrises: this avoids an influence of the previous night-time cooling and the next solar heating phase on the fits. The assumption of clear-sky conditions follows directly from the formulation of the DTC model (section 3.1.2.).

4.2. Constraints and Limitations

The TSP algorithm’s performance is influenced by the quality of the input LST as well as by atmospheric and surface wind conditions: therefore, the input LST data should at least approximate undisturbed DTC. However, relatively few DTC described by

MSG/SEVIRI pixel are retrieved under completely clear-sky conditions. Therefore, LSA SAF's operational processing chain uses DLST (LSA-003A) composites as input to the LSA-003B algorithm. Decadal LST composites are assumed to be statistically representative of their respective pixel and SEVIRI slot: this may not always be a realistic assumption, but a 10 day compositing period is a well-established compromise between resolving the dynamics at the surface and data availability (Holben, 1986). Consequently, the quality of the LSA-003A products is limited by the available observations for each pixel and time slot. However, spatial continuity is maximised by only requiring a single valid MLST for the composites to be formed. This can introduce substantial variability into the resulting 'synthetic DTC', but the effect of isolated outliers on the LSA-003B (TSP) algorithm is limited by the simultaneous fitting of the DTC model to the entire time series of LST composites, which smoothes short-term variability considerably (see section 0).

The minimum number of required input LST is determined by the number of free model parameters (TSP). However, this assumes that the information contained in the LST is not redundant, e.g. it is not possible to retrieve an entire DTC from night-time LST only. If the number of input LST is smaller than number of parameters, e.g. as quite common for polar orbiters, modelling may still be possible provided that the number of free parameters can be reduced (Schädlich et al., 2001).

5. References

- Bastiaanssen, W.G.M., Menenti, M., Feddes, R.A., and Holtslag, A.A.M. (1998). A remote sensing surface energy balance algorithm for land (SEBAL) 1. Formulation. *Journal of Hydrology*, 212–213 and 198–212.
- Basist, A., Grody, N.C., Peterson, T.C., and Williams, C.N. (1998). Using the Special Sensor Microwave/Imager to Monitor Land Surface Temperatures, Wetness, and Snow Cover. *Journal of Applied Meteorology*, Vol.37.
- Barbosa, P.M., Pereira, J.M.C., and Gegoire, J.-M. (1998). Compositing Criteria for Burned Area Assessment Using Multitemporal Low Resolution Satellite Data. *Remote Sensing of Environment*, Vol. 65, pp. 38–49.
- Baroncini, F., Castelli, F., Caparrini, F., and Ruffo, R. (2008). A dynamic cloud masking and filtering algorithm for MSG retrieval of land surface temperature. *International Journal of Remote Sensing*, 29(12), 3365–3382.
- Bosilovich, M. G., Radakovich, J. D., da Silva, A., Todling, R., and Verter, F. (2007). Skin temperature analysis and bias correction in a coupled land-atmosphere data assimilation system. *J. Meteorol. Soc. Japan*, vol. 85A, 205–228.
- Caparrini, F., Castelli, F., and Entekhabi, D. (2004). Variational estimation of soil and vegetation turbulent transfer and heat flux parameters from sequences of multisensor imagery. *Water Resour. Res.*, vol. 40, doi:10.1029/2004WR003358.
- Carlson, T.N., and Boland, F.E. (1978). Analysis of urban-rural canopy using a surface heat flux / temperature model. *Journal of Applied Meteorology*, 17, 999–1013.
- Carslaw, H.S., and Jaeger, J.C. (1959). Conduction of heat in solids. London: Oxford University Press
- Cautenet, G., Legrand, M., Cautenet, S., Bonnel, B., and Brogniez, G. (1992). Thermal impact of Saharan dust over land. Part I: simulation. *Journal of Applied Meteorology*, 31, 166–180.
- Cleugh, H.A., Leuning, R., Mu, Q., and Running, S.W. (2007). Regional evaporation estimates from flux tower and MODIS satellite data. *Remote Sensing of Environment*, Vol. 106, pp. 285–304.
- Cracknell, A.P., and Xue, Y. (1996). Thermal inertia determination from space: a tutorial review. *International Journal of Remote Sensing*, 17, 431–461.
- Dash, P., Göttsche, F.-M., Olesen, F.-S., and Fischer, H. (2002). Land surface temperature and emissivity estimation from passive sensor data: theory and practice; current trends. *International Journal of Remote Sensing*, 23, 2563–2594.
- Duan, S.-B., Li, Z.-L., Wang, N., Wu, H., and Tang, B.-H. (2012). Evaluation of six land-surface diurnal temperature cycle models using clear-sky in situ and satellite data. *Remote Sensing of Environment*, 124, 15–25.
- Freitas, S.C., Trigo, I.F., Bioucas-Dias, J.M., and Göttsche, F.-M. (2010). Quantifying the Uncertainty of Land Surface Temperature Retrievals from SEVIRI/Meteosat. *IEEE Transactions on Geoscience and Remote Sensing*, 48(1), 523–534.
- Göttsche, F.-M., Olesen, F.S., and Bork-Unkelbach, A. (2013). Validation of land surface temperature derived from MSG/SEVIRI with in situ measurements at Gobabeb, Namibia. *International Journal of Remote Sensing*, 34, 3069–3083.
- Göttsche, F.-M., and Olesen, F.S. (2001). Modelling of diurnal cycles of brightness temperatures extracted from METEOSAT data. *Remote Sensing of Environment*, 76, 337–348.

- Göttsche, F.-M., and Olesen, F.S. (2009). Modelling the effect of optical thickness on diurnal cycles of land surface temperature. *Remote Sensing of Environment*, 113, 2306–2316.
- Holmes, T. R. H., Crow, W. T., and Hain, C. (2014). Spatial patterns in timing of the diurnal temperature cycle. *Hydrol. Earth Syst. Sci.*, 17, 3695–3706.
- Holben, B. N. (1986). Characteristics of maximum-value composite images from temporal AVHRR data. *International Journal of Remote Sensing*, 7, 1417–1734.
- Inamdar, A.K., French, A., Hook, S., and Vaughan, G. (2008). Land surface temperature retrieval at high spatial and temporal resolutions over the southwestern United States. *Journal of Geophysical Research*, 113, D07107.
- Inamdar, A.K., and French, A., (2009). Disaggregation of GOES land surface temperatures using surface emissivity. *Geophysical Research Letters*, 36, L02408.
- Iqbal, M. (1983). An introduction to solar radiation. Toronto: Academic Press
- Jaeger, J.C. (1953). Conduction of heat in a solid with periodic boundary conditions, with an application to the surface temperature of the Moon. *Proceedings of the Cambridge Philosophical Society*, 49, 355–359.
- Jedlovec, G.J. Haines, S.L., and LaFontaine, F.J. (2008). Spatial and Temporal Varying Thresholds for Cloud Detection in GOES Imagery. *IEEE Transactions on Geoscience and Remote Sensing*, V. 46, N. 6.
- Jiang, G.-M., Li, Z.-L., and Nerry, F. (2006). Land surface emissivity retrieval from combined mid-infrared and thermal infrared data of MSG-SEVIRI. *Remote Sensing of Environment*, 105, 326–340.
- Jin, M. (2004). Analysis of land skin temperature using AVHRR observations. *Bull. Amer. Meteorol. Soc.*, 85, pp. 587–600.
- Jin, M., Dickinson, R.E., and Zhang, D. (2005). The Footprint of Urban Areas on Global Climate as Characterized by MODIS. *J. Climate*, vol. 18, 1551–1565.
- Julien, Y., Sobrino, J.A., and Verhoef, W. (2006). Changes in land surface temperatures and NDVI values over Europe between 1982 and 1999. *Remote Sensing of Environment*, Vol. 103, pp. 43–55.
- Kabsch, E., Olesen, F.S., and Prata, F. (2008). Initial results of the land surface temperature (LST) validation with the Evora, Portugal ground-truth station measurements. *International Journal of Remote Sensing*, 29, 5329–5345.
- Kalma, J.D., McVicar, T.R., and McCabe, M.F. (2008). Estimating Land Surface Evaporation: A Review of Methods Using Remotely Sensed Surface Temperature Data. *Surv Geophys*, Vol.29, pp.421–469.
- Kasten, F., and Young, A.T. (1989). Revised optical air mass tables and approximation formula. *Applied Optics*, 28(22), 4735–4738.
- Kogan, F.N. (1995). Application of vegetation index and brightness temperature for drought detection. *Advances in Space Research*, 15(11), 91–100.
- Kogan, F.N. (1997). Global drought watch from space. *Bulletin of the American Meteorological Society*, 78(4), 621–636.
- Kustas, W.P., and Daughtry, C.S.T. (1990). Estimation of the soil heat flux/net radiation ratio from spectral data. *Agricultural and Forest Meteorology*, 49, 205–223.
- Kustas, W. P., and Norman, J. M. (1996). Use of remote sensing for evapotranspiration monitoring over land surfaces. *Hydrol. Sci. J.*, vol. 41, pp. 495–515.
- Lambin, E.F., and Ehrlich, D. (1996). The surface temperature-vegetation index space for land cover and land-cover change analysis. *Int. J. Remote Sens.*, vol 17, 463–487.

- Lambin, E.F., and Ehrlich, D. (1997). Land-cover Changes in Sub-Saharan Africa (1982-1991): Application of a Change Index Based on Remotely Sensed Surface Temperature and Vegetation Indices at a Continental Scale. *Remote Sensing of Environment*, Vol.61, pp. 181–200.
- Land SAF Project Team (2010). Product User Manual Land Surface Temperature (LST), Prepared by the Land Surface Analysis Satellite Application Facility for EUMETSAT.
- Legrand, M., Cautenet, G., and Buriez, J.C. (1992). Thermal impact of Saharan dust over land. Part II: application to satellite IR remote sensing. *Journal of Applied Meteorology*, 31, 181–193.
- Legrand, M., Bertrand, J.J., Desbois, M., Menenger, L., and Fouquart, Y. (1989). The potential of infrared satellite data for the retrieval of Saharan-dust optical Depth over Africa. *Journal of Applied Meteorology*, 28, 309–319.
- Liebenthal, C., and Foken, T. (2007). Evaluation of six parameterization approaches for the ground heat flux. *Theoretical and Applied Climatology*, 88, 43–56.
- Lin, J.D. (1980). On the force-restore method for prediction of ground surface temperature. *Journal of Geophysical Research*, 85(6), 3251–3254.
- Liu, H.-Q., Duan, S.-B., Shao, K., Chen, Y., and Han, X.-J. (2015). Combining thermal inertia and a diurnal temperature difference cycle model to estimate thermal inertia from MSG-SEVIRI data. *International Journal of Remote Sensing*, 36, 4808–4819.
- McVicar, T.R., and Bierwirth, P.N. (2001). Rapidly assessing the 1997 drought in Papua New Guinea using composite AVHRR imagery. *International Journal of Remote Sensing*, Vol.22, pp. 2109–2128.
- Mildrexler, D.J., Zhao, M., Heinsch, F.A., and Running, S.W. (2007). A new satellite-based methodology for continental-scale disturbance detection. *Ecological Applications*, V.17, pp. 235–250.
- Mitchell, K. E. , Lohmann, D., Houser, P. R., Wood, E. F. , Schaake, J. C., Robock, A., Cosgrove, B. A., Sheffield, J., Duan, Q., Luo, L., Higgins, R. W., Pinker, R. T., Tarpley, J. D., Lettenmaier, D. P., Marshall, C. H., Entin, J. K., Pan, M., Shi, W., Koren, V., Meng, J., Ramsay, B. H., and Bailey, A. A. (2004). The multi-institution North American Land Data Assimilation System (NLDAS): Utilizing multiple GCIP products and partners in a continental distributed hydrological modeling system. *J. Geophys. Res.*, vol. 109, doi: 10.1029/2003JD003823.
- Neteler, M. (2005). Time Series Processing of MODIS Satellite Data for Landscape Epidemiological Applications. *International Journal of Geoinformatics*, Vol.1, No.1, ISSN 1686–6576.
- Nishida, K., Nemani, R.R., Running, S.W., and Glassy, J.M. (2003). An operational remote sensing algorithm of land surface evaporation. *Journal of Geophysical Research*, Vol.108, No. D9, 4270.
- Press, W.H., Flannery, B.P., Teukolsky, S.A., and Vetterling, W.T. (1990). *Numerical recipes in C*. Cambridge, New York: Cambridge University Press
- Price, J.C. (1977). Thermal inertia mapping: a new view of the Earth. *Journal of Geophysical Research*, 82, 2582–2590.
- Price, J.C. (1985). On the analysis of thermal infrared imagery: the limited utility of apparent thermal inertia. *Remote Sensing of Environment*, 18, 59–73.

- Price, J.C. (1989). Quantitative aspects of remote sensing in the thermal infrared. In: G. Asrar (Ed.), *Theory and applications of optical remote sensing* (pp. 578–603). New York: John Wiley & Sons
- Qin, J. , Liang, S., Liu, R., Zhang, H., and Hu, B. (2007). A Weak-Constraint-Based Data Assimilation Scheme for Estimating Surface Turbulent Fluxes. *IEEE Trans. Geosci. Remote Sens. Lett.*, vol. 4, doi: 10.1109/LGRS.2007.904004.
- Randolph, S., Green, R., Peacey, M. and Rogers, D., (2000). Seasonal synchrony: The key to tick-borne encephalitis foci identified by satellite data. *Parasitology*, Vol. 121, pp. 15–23.
- Reuter, M. (2005). Identification of cloudy and clear sky areas in MSG SEVIRI images by analyzing spectral and temporal information. *Ph.D. Thesis* , Freie Universität Berlin
- Rojas, O., Vrieling, A., and Rembold, F. (2011). Assessing drought probability for agricultural areas in Africa with coarse resolution remote sensing imagery. *Remote Sensing of Environment*, 115, 343–352.
- Roy, D.P. (1997). Investigation of the maximum Normalized Difference Vegetation Index (NDVI) and the maximum surface temperature (Ts) AVHRR compositing procedures for the extraction of NDVI and Ts over forest. *International Journal of Remote Sensing*, Vol.18, No.11, pp.2383–2401.
- Sandholt, I., Rasmussen, K., and Andersen, J. (2002). A simple interpretation of the surface temperature / vegetation index space for assessment of surface moisture status. *Remote Sensing of Environment*, Vol. 79, pp. 213–224.
- Schädlich, S., Göttsche, F.-M., and Olesen, F.-S. (2001). Influence of land surface parameters and atmosphere on METEOSAT brightness temperatures and interpolation of atmospheric correction. *Remote Sensing of Environment*, 75(1), pp. 39–46.
- Schoenberg, E. (1929). Theoretische Photometrie, g) Über die Extinktion des Lichtes in der Erdatmosphäre. In: Bottlinger et al. (Ed.), *Handbuch der Astrophysik, Band II/1*. Berlin: Springer.
- Schmetz., J., Pili, P., Tjemkes, S., Just, D., Kerkman, J., Rota, S., and Ratier, A. (2002). An introduction to Meteosat Second Generation (MSG). *Bull. Amer. Meteor. Soc.*, vol. 83, 977–992.
- Singh, R.P., Roy, S., and Kogan, F. (2003). Vegetation and temperature condition indices from NOAA AVHRR data for drought monitoring over India. *International Journal of Remote Sensing*, 20(22), 4393–4402.
- Stöckli, R. (2013). The HelioMont Surface Solar Radiation Processing, *Scientific Report MeteoSwiss*, 93, ISSN: 1422–138, 122 pp.
- Stoll, M.P. (1994). Potential of remote sensing in the thermal band for global change. In: Vaughan, R.A., & Cracknell, A.P. (Ed.), *Remote sensing and global climate change, NATO Advanced Science Institutes Series, Series I, 24* (pp. 393–404). Berlin: Springer Verlag
- Tanre, D., and Legrand, M. (1991). On the satellite retrieval of Saharan dust optical thickness over land: two different approaches. *Journal of Geophysical Research*, 96(D3), pp. 5221–5227.
- Trigo, I. F., and Viterbo, P. (2003). Clear-Sky Window Channel Radiances: A Comparison between Observations and the ECMWF Model, *J. Appl. Meteor.*, vol. 42, pp. 1463–1479.

- Trigo, I., Freitas, S., Bioucas-Dias, J. Barroso, C. Monteiro, I., and P. Viterbo (2009). Algorithm Theoretical Basis Document for Land Surface Temperature (LST), Prepared by the Land Surface Analysis Satellite Application Facility (LSA SAF) for EUMETSAT.
- Trigo, I.F., Freitas, I. Monteiro, S. Coelho, F., Olesen, E. Kabsch, and F. Götsche (2009a). SAF for Land Surface Analysis (LSA SAF) Validation Report LST, Prepared by the Land Surface Analysis Satellite Application Facility for EUMETSAT.
- Vollmer, M., and Gedzelmann, S.D. (2006). Colours of the Sun and Moon: the role of the optical air mass. *European Journal of Physics*, 27, pp. 299–309.
- Wan, Z., Wang, P., and Li, X. (2004). Using MODIS land surface temperature And Normalized DifferenceVegetation Index products for monitoring drought in the southern Great Plains, USA. *Int J. Remote Sens.*, vol. 25, pp. 61–72.
- Watson, K. (1973). Periodic heating of a layer over semi-infinite solid. *Journal of Geophysical Research*, 78, pp. 5904–5910.
- Watson, K., and Hummer-Miller, S. (1981). A simple algorithm to estimate the effective regional atmospheric parameters for thermal-inertia mapping. *Remote Sensing of Environment*, 11, pp. 455–462.
- Watson, K. (1999). A diurnal animation of thermal images from a day-night pair. *Remote Sensing of Environment*, 72, pp. 237–243.
- Wetzel, P.J., Atlas, D., and Woodward, R.H. (1984). Determining soil moisture from geosynchronous satellite infrared data: a feasibility study. *Journal of Applied Meteorology*, 23(3), pp. 375–391.
- Yee, S.Y.K. (1988). The force restore method revisited. *Boundary-Layer Meteorology*, 43, pp. 85–90.
- Yu, Y., Privette, J. L., and Pinheiro, A. C. (2008). Evaluation of Split-Window Land Surface Temperature Algorithms for Generating Climate Data Records. *IEEE Trans. Geosci. Remote Sens.*, vol. 46, doi: 10.1109/TGRS.2007.909097.

Annex - Derived LST Composite Products: LSA-003 (DLST) Processing Scheme

The derived DLST composite products are directly created from LSA-001 products (MLST), i.e. DLST pixel consist of selected MSG/SEVIRI LST retrieved with the MLST algorithm (sections **Erro! A origem da referência não foi encontrada.** and **Erro! A origem da referência não foi encontrada.**). Only valid MLST data within the compositing period are taken into account and processing is performed for the entire MSG/SEVIRI disk. Before DLST composite products can be formed, the MLST input files for the compositing period have to be available: therefore, for decadal composites the MLST files of the previous 10 days, i.e. up to 960 (1056 for 11 days) MLST files have to be kept in the processing chain. Separate algorithms for median and maximum LST composites have been implemented. The main steps of DLST algorithm execution may be described as follows:

LSA-003A

Maximum LST Composite:

- 1 outer loop over the 96 daily MSG slots (time)
- 2 inner loop over the input files matching current MSG slot (time)
 - 2.1 outer loop over MSG line
 - 2.2 inner loop over MSG column
 - 2.2.1 obtain number of valid LST
 - 2.2.2 save LST maximum and respective QC flag & error bar

Median LST Composite:

- 1 outer loop over the 96 daily MSG slots (time)
- 2 inner loop over the input files matching current MSG slot (time)
 - 2.1 store LST and error bar as layers in 3-D array
- 3 outer loop over MSG line
- 4 inner loop over MSG column
 - 4.1 extract all valid LST at location (column, line) from 3-D array
 - 4.2 obtain median LST, error bar and number of valid LST

The Thermal Surface Parameters (TSP) model is then applied to the output of LSA-003A, allowing the description of the median and maximum LST diurnal cycle (96 time-slots) over each 10-day period using 7 parameters, of which 6 are free:

LSA-003B

Thermal Surface Parameters (TSP):

- 1 load up to 96 DLST composites (LSA-003A) as layers into 3-D array
- 2 outer loop over MSG line
- 3 inner loop over MSG column
 - 3.1 extract 'synthetic' DTC at (column, line) from 3-D array
 - 3.2 initialize TSP based on DTC statistics
 - 3.3 fit the model to the DTC (max. 10 iterations)
 - 3.4 if stop criterion is met, save TSP, errors, and QC flags

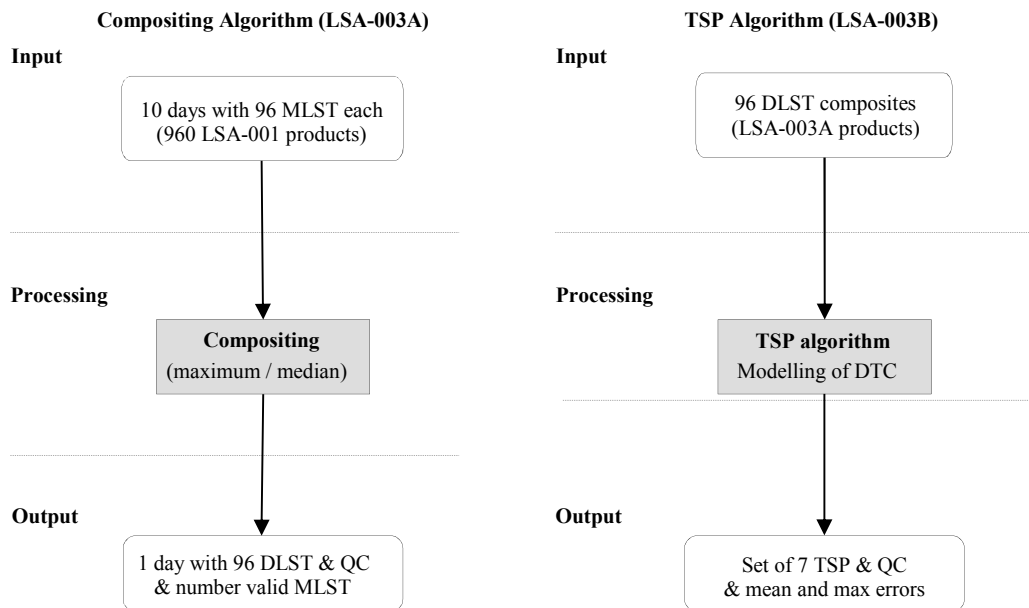


Figure 21 Processing chains of the derived LST (DLST) product (LSA-003). Left: Temporal LST composites (LSA-003A). Right: Thermal Surface Parameters (TSP) algorithm (LSA-003B). The TSP algorithm fits a model of the diurnal temperature cycle (DTC) to DLST composites. The DTC model and the TSP are explained in Figure 6 and Table 2.